

Supplemental Data

Tumor heterogeneity and immune-evasive T follicular cell lymphoma phenotypes at single-cell resolution

Sakurako Suma¹, Yasuhito Suehara¹, Manabu Fujisawa^{2,3}, Yoshiaki Abe², Keiichiro Hattori^{1,2}, Kenichi Makishima¹, Tatsuhiko Sakamoto^{1,2}, Aya Sawa⁴, Hiroko Bando⁴, Daisuke Kaji⁵, Takeshi Sugio⁶, Koji Kato⁷, Koichi Akashi⁷, Kosei Matsue⁸, Joaquim Carreras⁹, Naoya Nakamura⁹, Ayako Suzuki¹⁰, Yutaka Suzuki¹⁰, Ken Ito¹¹, Hiroyuki Shiiba¹², Shigeru Chiba^{1,2}, and Mamiko Sakata-Yanagimoto^{1,2,13}

¹ Department of Hematology, University of Tsukuba Hospital, Tsukuba, Japan.

² Department of Hematology, Institute of Medicine, University of Tsukuba, Tsukuba, Japan.

³ Centre for Lymphoid Cancer, BC Cancer, Vancouver, BC, Canada.

⁴ Department of Breast-Thyroid-Endocrine Surgery, University of Tsukuba Hospital, Tsukuba, Japan.

⁵ Department of Hematology, Toranomon Hospital, Tokyo, Japan.

⁶ Department of Medicine, Division of Oncology, Stanford University, Stanford, CA, USA.

⁷ Department of Medicine and Biosystemic Science, Kyushu University Graduate School of Medical Science, Fukuoka, Japan.

⁸ Division of Hematology/Oncology, Department of Internal Medicine, Kameda Medical Center, Kamogawa, Japan.

⁹ Department of Pathology, Tokai University School of Medicine, Isehara, Japan.

¹⁰ Department of Computational Biology and Medical Sciences, the University of Tokyo, Kashiwa, Japan.

¹¹ Oncology Business Unit, Eisai Co., Ltd., Tsukuba, Japan.

¹² Oncology Department, Medical Head Quarters, Eisai Co., Ltd., Tokyo, Japan.

¹³ Division of Advanced Hemato-Oncology, Transborder Medical Research Center, University of Tsukuba, Tsukuba, Japan.

Supplementary Methods

Supplementary Notes

Supplementary Table Legends

Supplementary Figures (with legends)

1 **Supplementary Methods**

2 **Patients and clinical sample collection**

3 Lymph node (LN) and peripheral blood (PB) samples were collected from 14 patients with
4 T follicular helper cell (T_{FH}) lymphomas (TFHLs) at the University of Tsukuba Hospital, Kameda
5 Medical Center (Kamogawa, Japan), and Toranomom Hospital (Tokyo, Japan) between October
6 of 2019 and February of 2021. For two of the TFHL patients (AITL1 and AITL2), PB samples
7 were collected at two-time points: once upon new diagnosis (ND) (AITL1_{ND} and AITL2_{ND}) and
8 again upon refractory/relapsed (RR) disease (AITL1_{RR} and AITL2_{RR}). LN samples from AITL5
9 and AITL7 were analyzed in a previously reported study [1]. For single-cell RNA sequencing
10 (scRNA-seq) data from AITL4, only tumor cells were analyzed because systemic steroid
11 administration for coexisting collagen disease may affect the composition of immune cells.
12 Additionally, seven homeostatic LN (HLN) samples were also collected from patients with non-
13 hematological malignancies at the University of Tsukuba Hospital and were confirmed as
14 metastatic-free by flow cytometric (FCM) analysis of pan-cytokeratin. The patient characteristics
15 are summarized in Table S1.

16

17 **Sample processing**

18 LN samples were minced immediately after excision and filtered with a 70- μ m strainer.
19 The cells were washed with phosphate-buffered saline (PBS, Nissui, Tokyo, Japan), containing
20 0.04% weight/volume bovine serum albumin (BSA, Sigma-Aldrich, Louis, MO, USA), and
21 centrifuged twice for 5 min at $300 \times g$ and 4°C. After removal of the supernatant, cells were
22 resuspended in PBS/0.04% BSA and cell count and viability were estimated using a
23 hemocytometer and trypan blue. After centrifugation for 5 min at $300 \times g$ and 5°C once again,

24 cells were resuspended in PBS/0.04% BSA and diluted to 1×10^7 cells/ml in preparation for
25 analysis or cryopreservation.

26 PB samples were stored at 4°C immediately after collection and processed within 24 h.
27 After red blood cell (RBC) lysis by the ammonium-chloride-potassium buffer, cells were washed
28 once with PBS/0.04% BSA and centrifuged for 5 min at $400 \times g$ and 4°C. After removal of the
29 supernatant, cells were resuspended in 20 ml of PBS/0.04% BSA buffer and cell count and
30 viability were estimated. Cells were centrifuged for 5 min at $300 \times g$ and 4°C, diluted to 1×10^7
31 cells/ml and kept on ice until use.

32

33 **FCM analysis and sorting**

34 Surface protein expression analysis and sorting for scRNA-seq were performed using cell
35 suspensions obtained from the LN and PB samples described above. To prevent non-specific
36 reactions mediated by Fc receptors (FcRs), 20 μ l/ 10^7 cells of FcR Blocking Reagent (Miltenyi
37 Biotec, Bergisch Gladbach, Germany) was added, and cell suspensions were incubated in a
38 refrigerator for 10 min, followed by staining based on the recommended concentration of each
39 antibody. Dead cells and doublets were removed by 7-amino-actinomycin D (7-AAD, Thermo
40 Fisher Scientific, Waltham, MA, USA) staining and forward versus side scatter plots (Fig. S1A–
41 B). FCM sorting and analysis were performed on BD FACSAria III (BD Biosciences, San Jose,
42 CA, USA). FlowJo software (v10.7.1, Tree Star Inc., Ashland, OR, USA) and the Ggplot2
43 package (v3.3.3) [2] were used for FCM data analysis and visualization. All antibodies used are
44 listed in Table S20.

45

46 **Library preparation, sequencing, and pre-processing of single-cell data**

47 The scRNA-seq libraries for mononuclear cells (MNCs) from LNs and PB were prepared
48 using a Chromium Single Cell 5' Library & Gel Bead Kit (v1 chemistry, 10x Genomics,
49 Pleasanton, CA, USA) or a Chromium Next GEM Single Cell 5' Library & Gel Bead Kit (v1.1
50 chemistry) according to the manufacturer's instructions (CG000086 Rev L or CG000207 Rev
51 E), aiming for 5 000 cells per library. Simultaneously, single-cell T- and B-cell receptor
52 sequencing (scTCR/BCR-seq) was performed for samples with sufficient T or B cells (> 20% of
53 all LN MNCs or > 10% of all PB MNCs; Table S1 and S4). scTCR/BCR-seq libraries were
54 constructed using a Chromium Single Cell V(D)J Reagent Kit (v1 or v1.1 chemistry). T cell-
55 enriched scRNA/TCR-seq libraries were generated similarly to the MNCs using sorted
56 CD4/CD8⁺ T cells. Quantification and quality control of libraries were performed using a 2100
57 Bioanalyzer System with High Sensitivity DNA Kit (Agilent Technologies, Santa Clara, CA,
58 USA) and a KAPA Library Quantification Kit for Illumina platforms (KAPA Biosystems,
59 Wilmington, MA, USA). Each cDNA library was sequenced on the HiSeq X system (Illumina,
60 San Diego, CA, USA) with a paired-end 150-base read option. The publicly available 5'
61 scRNA-seq and scTCR/BCR-seq data from PB of 5 healthy donors (HDs) [3] generated by a
62 Chromium system (Chromium Single Cell 5' Reagent Kit v2 chemistry and Chromium Single
63 Cell V(D)J Reagent Kit) were used as controls (Table S1). The age and sex of individual donors
64 were obtained from Supplementary Figure S1 of the original paper [3].

65 Using the "cellranger count" function of the Cell Ranger pipeline (v3.1.0, 10x
66 Genomics), we aligned scRNA-seq data to the reference genome (GRCh38) and performed
67 preliminary filtering and counting unique molecular identifiers (UMIs) for downstream analysis.
68 For scTCR/BCR-seq data, sequence assembly and paired clonotype calling were performed
69 with the "cellranger vdj" function. scRNA-seq and scTCR/BCR-seq data, after implementing

70 the Cell Ranger pipeline, were primarily analyzed using R (v3.6.0, v3.6.2 or v4.0.2) on RStudio
71 (v1.2.1578 or v1.2.5019).

72

73 **Quality control (QC) of scRNA-seq data**

74 First, to remove low-quality cells and genes, only genes expressed by more than three
75 cells and cells expressing over 200 genes were included in further analyses. Next, we applied
76 the Scater package (v1.14.6) [4] to filter out outliers from count matrices for each sample.
77 Briefly, we used several common QC metrics to detect outliers: library size, which was defined
78 as the total sum of counts across all relevant features for each cell; the number of expressed
79 features in each cell; and the percentage of reads mapped to mitochondrial transcripts. Outliers
80 were identified based on the median absolute deviation from the median value of each QC
81 metric across all cells. Cells identified as outliers were considered to be low quality and
82 discarded. After excluding mitochondrial and ribosomal genes, the Seurat package (v3.2.3) [5,6]
83 was applied to log-normalize the count data by the default scale factor of 10 000.

84

85 **Batch effects correction and data integration**

86 The mutual nearest neighbors (MNN) batch correction technique in the Batchelor
87 package (v1.2.4) [7] was utilized to remove batch effects between datasets resulting from
88 technical biases and biological differences. Unlike the original method, the
89 “batchelor::fastMNN” function performs principal components analysis (PCA) on the
90 previously selected highly variable features (HVF) to preemptively reduce the dimensions and
91 speed up MNN identification and correction. For integrating data from LNs of patients with
92 TFHL and HLNs, we used 2 000 HVFs and the first 50 principal components (PCs) for

93 downstream steps. For data from PB, 3 000 HVFs and the first 100 PCs were used instead. In
94 LN data, variable genes of TCR $\alpha\beta$ and immunoglobulins (*TRAV*, *TRBV*, *IGHV*, *IGKV*, and
95 *IGLV*) were removed from the HVF selection to avoid their effect on clustering. We applied the
96 “RunFastMNN” function in the SeuratWrappers package (v0.3.0;
97 <https://github.com/satijalab/seurat-wrappers>) for running the “fastMNN” function with a Seurat
98 object.

99

100 **Unsupervised clustering and non-linear dimensional reduction**

101 Subsequently, we applied Seurat to perform unsupervised graph-based clustering and
102 Uniform Manifold Approximation and Projection (UMAP) visualization using the MNN-
103 corrected components as input. Using the “FindNeighbors” function, a k-nearest neighbor graph
104 was constructed based on the Euclidean distance and a shared nearest neighbor graph was
105 generated by computing the neighborhood overlap between any two cells. Next, the
106 “FindClusters” function was used to identify clusters by the Louvain algorithm (default setting),
107 which was a shared nearest neighbor modularity optimization-based clustering algorithm. For
108 visualization, UMAP transformation was performed using the “RunUMAP” function.

109

110 **Finding cluster biomarkers and cell type annotation**

111 To characterize each cluster, we used the “FindMarkers” or “FindAllMarkers” functions
112 in the Seurat package to select upregulated genes in each cluster relative to other clusters. These
113 functions performed the Wilcoxon Rank Sum test between pairs of clusters and a *P*-value
114 adjustment using the Bonferroni correction. Clusters were manually assigned to a cell type by
115 comparing the marker genes of each cluster and known canonical markers. Specifically, we

116 annotated CD3 gene (*CD3D*, *CD3E*, and *CD247*)- and *CD4* or *CD8* gene (*CD8A* and *CD8B*)-
117 positive clusters as "CD4/CD8⁺ T cells", *CD79A*-positive clusters as "B cells," and myeloid cell
118 marker (*LYZ*, *CD68*, and *CST3*) [8,9]-positive clusters as "myeloid cells." CD3 gene-positive or
119 weakly positive but *CD4* and *CD8* gene-negative and natural killer (NK) cell marker (*XCL1*,
120 *FCGR3A*, *KLRD1*, and *KLRF1*) [10]- or $\gamma\delta$ T cell marker (*TRDV2*, *TRGV9*, *TRDC*, *TRGC2*, and
121 *TRGCI*) [11]-positive clusters were named as "NK cells" (for LNs) or "NK/ $\gamma\delta$ T cells" (for PB
122 samples). We also identified a *CD34*-positive "progenitor cell" cluster as a rare cell type (81
123 cells in all PB MNCs) in PB. Platelet clusters characterized by *PPBP*, *GP9*, and *PF4* and RBC
124 clusters characterized by *HBB* and *HBAI* were excluded from downstream analyses. For
125 clusters featured by the expression of multiple cell-type marker genes, we used the scDblFinder
126 package (v1.4.0) [12] and confirmed that most cells in these clusters were doublets. These cells
127 were also removed from further analysis.

128 Subsequently, after identifying tumor cells by the method described below, we
129 subclustered immune cells by major cell types and annotated each cluster based on canonical
130 markers. Results of manual annotations were confirmed by automated annotation by the
131 SingleR package (v1.4.1) [13] with reference to previously published single-cell data.

132

133 **Single-cell TCR/BCR repertoire analysis**

134 We identified clonotypes from scTCR/BCR-seq data after running the Cell Ranger pipeline.
135 Clonotypes were identified by sets of cells with unique and "productive" TCR α - and/or β -chains
136 (for B cells, immunoglobulin [Ig] heavy [IgH] chains and two types of light [IgL] chains: κ or λ
137 [IgK or IgL] chains), defined by identical complementarity-determining region 3 (CDR3)
138 sequences. Here, a "productive" sequence refers to an mRNA sequence that could be translated
139 into a functional protein. Those TCR- or Ig-chain sequences judged as productive met the

140 following conditions: were full length (include from the beginning of the V gene to the end of the
141 J gene), started with a start codon, contained no stop codon, were in-frame, contained a CDR3
142 sequence, and matched the structural requirements calculated from the length of the V and J gene
143 regions of the sequence ([https://support.10xgenomics.com/single-cell-
144 vdj/software/pipelines/3.1/algorithms/annotation](https://support.10xgenomics.com/single-cell-vdj/software/pipelines/3.1/algorithms/annotation)). These clonotypes were named clonotype 1,
145 clonotype 2, and so on from the most clonally extended ones for each sample. Generally, $\alpha\beta$ T and
146 B cells express a pair of functional α - and β -chains or H- and L-chains but, occasionally, a single
147 cell expresses multiple functional TCR or Ig chains [14–17]. Therefore, we detected up to two
148 productive TCR α - and β -chains (IgH- and L-chains) in each cell. Downstream analysis of
149 scTCR/BCR-seq was performed using the Immunarch package (v0.6.6) [18].

150

151 **Tumor cell detection in TFHL LNs and PB**

152 For LNs, we defined clonotypes that were expressed by over 20 CD4⁺ T cells and
153 accounted for over 1.5% of all T cells with TCRs as “major tumor-cell clonotypes” and cells
154 with tumor-cell clonotypes as “tumor cells” (Fig. 1C; Table S3). Clonotypes composed only of
155 the TCR α - and/or β -chains identical to the major tumor-cell clonotypes and expressed by five
156 or more CD4⁺ T cells were defined as “minor tumor-cell clonotypes.” Cells expressing a minor
157 tumor-cell clonotype were also defined as tumor cells. Major and minor tumor-cell clonotypes
158 with the same TCR chains were grouped together as “tumor-clone subgroups” (Table S3).

159 In nine PB samples, with their paired LNs also subjected to single-cell sequencing, cells
160 harboring identical clonotypes to those of their respective LN tumor cells were defined as tumor
161 cells (Fig. S16A). In the remaining seven PB samples without paired LN single-cell data,
162 clonotypes that were expressed by over 100 cells and accounted for more than 10% of all TCRs
163 were defined as tumor-cell clonotypes. In patients with TFHL with sequential samples (AITL1

164 and AITL2), cells expressing the clonotypes identical to those of tumor cells of the sequential
165 sample were defined as tumor cells, even if no clonotype met the definition above (Fig. S16B).

166

167 **Differentially expressed gene (DEG) analysis**

168 We performed DEG analysis using the “FindMarkers” or “FindAllMarkers” functions of
169 Seurat. The model-based analysis of single-cell transcriptomics (MAST, v1.12.0) [19] method
170 was mainly used for DEG detection, and *P*-values were corrected by the Bonferroni method. In
171 addition, the Wilcoxon rank sum test confirmed the DEGs detected by MAST. Genes with an
172 adjusted *P*-value < 0.05 in both tests, with a log fold-change (logFC) of the average expression
173 between the two groups ≥ 0.15 (logfc.threshold = 0.15), and expressed by $\geq 10\%$ of cells in the
174 cluster (min.pct = 0.1) were considered significant. An adjusted *P*-value calculated by MAST
175 was used to create a volcano plot. Metascape [20] and gene set enrichment analysis (GSEA;
176 v4.1.0) [21] were used for gene ontology (GO) and pathway analyses of DEGs in specific
177 clusters, respectively.

178

179 **Gene set variation analysis (GSVA)**

180 The GSVA package (v1.34.0) [22] was applied to estimate signatures or pathways
181 enriched by each cell and cluster. The normalized data after log transformation was used as
182 input, and the Gaussian kernel was selected as the kernel function used for the nonparametric
183 estimation of enrichment scores for each cell. Gene sets for GSVA were downloaded from the
184 Molecular Signatures Database (MSigDB; <http://www.gsea-msigdb.org/gsea/msigdb/index.jsp>)
185 or extracted from a previously published RNA-seq dataset by DEG analysis using the edgeR
186 package (v3.28.1) [23,24]. We used raw count data as input for DEG analysis by edgeR, filtered

187 out low-expression genes using the “filterByExpr” function, performed trimmed mean of M-
188 values (TMM) normalization using the “calcNormFactors” function, and applied a generalized
189 linear model (GLM) using the likelihood ratio test (LRT) with the “glmLRT” function. DEGs
190 with an adjusted P -value < 0.05 and $\log_{2}FC \geq 1$ were extracted by the “decideTests” function.
191 Finally, we performed the pairwise Wilcoxon test and Bonferroni P -value correction using the
192 rstatix package (v0.7.0) [25] to compare median GSVA enrichment scores for each cluster.

193

194 **Trajectory analysis**

195 Trajectory analysis was performed using the Monocle2 (v2.18.0) [26], Monocle3
196 (v0.2.3.0) [27], and Slingshot (v1.8.0) [28] packages. The count data before normalization after
197 QC was used as the input data for Monocle2. After estimating size factors and dispersions with
198 the “estimateSizeFactors” and “estimateDispersions” functions, DEGs for each cluster were
199 extracted with the “differentialGeneTest” function. Using only DEGs with a P -value < 0.01 , the
200 “reduceDimension” function performed a DDRTree reduction, and the “orderCells” function
201 sorted the cells in trajectory order. In the Monocle3 analysis, we first converted the Seurat
202 object to a “cell_data_set” object that could be used in Monocle3 by the “as.cell_data_set”
203 function. After clustering with the “cluster_cells” function, trajectory estimation and cell sorting
204 were performed using the “learn_graph” and “orderCells” functions, using the results of
205 dimensional reduction by UMAP executed by Seurat. In trajectory analysis by Slingshot, after
206 converting the Seurat object to a “SingleCellExperiment” object using the
207 “as.SingleCellExperiment” function, dimensionality reduction data after batch effect correction
208 by fastMNN and clustering results by Seurat were used. Trajectory estimation was performed
209 by the “slingshot” function. We used the rgl package (v0.107.14,
210 <https://github.com/dmurdoch/rgl>) for 3D plots.

211

212 **Cell-cell interaction analysis**

213 Ligand-receptor interactions between each cluster were estimated using the Python
214 package CellPhoneDB (v3.0.0) [29] and the R package NicheNetR (v1.0.0) [30]. We used
215 Python v3.8.5 for this analysis. In the CellPhoneDB analysis, we first performed the “statistical
216 method” and obtained *P*-values. Specifically, only ligand-receptor pairs expressed by over 10%
217 of the cells in each cluster were selected for analysis. Then, we randomly permuted the cluster
218 labels of all cells 1 000 times to create a null distribution of the mean of the average ligand and
219 receptor expression levels in the interacting clusters. *P*-values for the probability of enrichment
220 within clusters for each ligand-receptor complex were obtained by calculating the percentage of
221 the means equal to or higher than the actual mean. Subsequently, we performed the “DEGs
222 analysis method,” using DEGs upregulated in each cluster of LNs from patients with ND or RR
223 TFHL versus HLNs as the input genes of the DEG list. As for CD8 T_{DYS} (T9), since the number
224 of cells belonging to CD8 T_{DYS} of HLNs was too small to perform proper DEG analysis, we
225 compared them with CD8 T_{EFF} (T8) of HLNs. Genes whose expression profiles were
226 significantly elevated in the tumor cells versus non-malignant cells were used as the DEGs for
227 the tumor cells. In the “DEGs analysis method,” only ligand-receptor pairs expressed by over
228 10% of the cells in each cluster and for which at least one gene was included in the DEG list
229 were extracted as significant interactions. Finally, interactions detected as significant by both
230 methods were extracted and the numbers of interactions for each cluster were plotted in
231 heatmaps.

232 NicheNetR is a tool for predicting ligands that can promote gene expression changes in
233 specific target cells (“receiver/target”). In this analysis, the group of genes representing gene
234 expression changes in target cells was defined as a “gene set of interest (geneset_oi).” The CD8

235 T_{DYS} (T9) cluster and tumor cells from RR TFHL were set as receivers and senders,
236 respectively. Initially, genes expressed by over 10% cells in each cluster designated as a
237 receiver or sender were used as “expressed_genes_receiver” and “expressed_genes_sender,”
238 respectively. Since the number of cells belonging to CD8 T_{DYS} of HLN was too small to
239 perform proper DEG analysis, DEGs between CD8 T_{DYS} of RR TFHL LN and CD8 T_{EFF} (T8)
240 of HLN with an adjusted *P*-value < 0.05, min.pct = 0.1, and logFC ≥ 0.35 were used as
241 “geneset_oi.” Next, we used the “predict_ligand_activities” function to estimate and rank the
242 potential ligands of target genes in “geneset_oi.” Among the potential ligands, the top 20 were
243 used as the “best_upstream_ligands” for the following analysis. Furthermore, the
244 “get_weighted_ligand_target_links” and “lr_network” functions predicted target genes and
245 receptors of the “best_upstream_ligands.” Finally, only bonafide interactions based on validated
246 curated ligand-receptor databases were visualized in heatmaps.

247

248 **Whole-exome sequencing (WES) and data processing**

249 Genomic DNA were extracted from fresh frozen tumor tissue and PB samples, formalin-
250 fixed paraffin-embedded (FFPE) tumor samples, and paired buccal swab samples to be used as
251 reference using a QIAamp DNA Blood Mini Kit or GeneRead DNA FFPE Kit (Qiagen, Hilden,
252 Germany) (Table S1). After DNA integrity number (DIN) values were measured using Agilent
253 TapeStation 2200 (Agilent Technologies) for quality control, DNA was fragmented with DNA
254 Shearing S220 (Covaris, Woburn, MA, USA). Exome capturing was performed using a
255 SureSelect XT Human All Exon V7 kit (Agilent Technologies). Next, 150-bp paired-end
256 sequencing was carried out according to the manufacturer’s recommendations on a HiSeq X
257 Ten system (Illumina).

258 Sequencing reads were aligned to the reference genome (GRCh37) using the Burrows-
259 Wheeler Aligner (v.0.7.8). Mutation calling was performed using the Genomon2 pipeline
260 (v.2.6.2, <https://github.com/Genomon-Project>) as previously described [1,31,32] with minor
261 modifications. Putative somatic mutations with a Fisher's exact P -value < 0.01 or an EB call P -
262 value > 2.0 , sequencing depth ≥ 30 , and variant reads > 4 were adopted. Furthermore, variants
263 only in unidirectional reads; variants in repetitive genomic regions; variants in intergenic,
264 intronic, untranslated, and noncoding RNA regions; and synonymous single-nucleotide variants
265 were excluded. Additionally, known recurrently mutated genes in TFHL, including *RHOA*
266 *G17V*, *TET2*, *DNMT3A*, and *IDH2*, were manually screened for as additional mutations.
267 Mapping errors were excluded by visual inspection with Integrative Genomics Viewer (IGV)
268 [33]. Detected somatic mutations are listed in Table S5.

269 Somatic copy number variations (CNVs) were analyzed by the Genome Analysis Tool Kit
270 (GATK; v4.2, Broad Institute, Cambridge, MA, USA) [34]. Buccal samples were used as a
271 panel of normals. The interval list was generated from the target browser extensible data (BED)
272 file of the SureSelect XT Human All Exon V7 kit downloaded from the Agilent website
273 (<https://earray.chem.agilent.com/suredesign/index.htm>). Gains and losses less than 1 Mb in
274 length were removed from downstream analyses.

275

276 **Inferring genetic mutations using scRNA-seq data**

277 We applied VarTriX (v1.1.16, 10x Genomics, <https://github.com/10XGenomics/vartrix>) to
278 extract single-cell variant information from scRNA-seq data. First, BED files of the somatic
279 mutations extracted by the Genomon2 pipeline for WES data were lifted from GRCh37 to
280 GRCh38 with the UCSC web browser (<https://genome.ucsc.edu/cgi-bin/hgLiftOver>). Then, the
281 BED files converted to variant call format (VCF) were used as input for VarTriX. We ran the

282 “vartrix” command with --mapq 255, --padding 100, and --umi mode options using a cell barcode
283 file extracted from the integrated Seurat object and a binary alignment map (BAM) file generated
284 by the Cell Ranger pipeline for each sample. Briefly, local sequence alignment at the input variant
285 locus was performed by the Smith-Waterman algorithm, and then wild-type and mutant reads
286 were counted for each cell, respectively. In --umi mode, a consensus is taken across each UMI,
287 and only cases where each UMI exceeded a hardcoded 90% threshold for supporting the same
288 allele were reflected in the results. Owing to the phenomenon commonly occurring in scRNA-
289 seq called “allelic dropout” (insufficient amplification of one allele), it is impossible to judge
290 whether a cell is a “truly wild type (WT)” in the absence of mutant reads [35]. Therefore, we
291 defined a cell as “unknown” if only WT reads or no reads were detected. Cells from THFL patients
292 without WES-identified mutations were classified as “WT” cells.

293

294 **Estimation of CNVs at the single-cell level**

295 To infer large-scale CNVs from scRNA-seq data, we applied the R package inferCNV
296 (v1.10.1). [36] Non-malignant T cells from each sample were used as controls for analysis of
297 PB and LN tumor cells. We used the following parameters: default de-noise and hidden Markov
298 model (HMM) setting, cutoff = 0.1, cluster_by_groups = FALSE, analysis_mode =
299 ‘subclusters’, and tumor_subcluster_partition_method = ‘random_trees’. Specifically, after
300 removing noise with the default settings, the random trees method was used to divide cells into
301 groups with consistent CNV patterns, and CNV prediction by HMM was performed at the
302 subcluster level. Uphyloplot2 (v2.3) [37] was applied to visualize phylogenetic trees using the
303 inferCNV output of each sample. CNV scores for each cell were calculated as previously
304 described [38].

305

306 **Immunohistochemical (IHC) staining**

307 Regarding *PLS3*, which was identified as a candidate tumor cell-specific gene, IHC
308 staining using FFPE samples of tumor tissues was performed by either the Tsukuba Human
309 Tissue Biobank Center Tsukuba Pathological Analysis Support Service (T-PASS, Tsukuba,
310 Japan) or expert hematopathologists at Tokai University School of Medicine. After antigen
311 retrieval with Target Retrieval Solution pH 9.0 (Dako, Santa Clara, CA, USA) using the
312 automated pretreatment system PT Link (Dako; 97°C, 20 min), anti-PLS3 antibody (Sigma-
313 Aldrich) diluted 1:100 was added, and samples were stained with Autostainer Link 48 (Dako).
314 PLS3 staining was determined to be positive when 10% or more of the cells were positive.

315

316 **High-dimensional spatial analysis by imaging mass cytometry (IMC)**

317 Carrier-free antibodies were manually conjugated to metal isotopes using the MaxPar 8X
318 antibody labeling kit (Standard BioTools Inc., South San Francisco, CA, USA) following the
319 manufacturer's protocol (Maxpar Antibody Labeling Kit PRD002 Version 11). Manually
320 conjugated or pre-metal-tagged antibodies obtained from Standard BioTools Inc. were used for
321 IMC staining (Table S17). FFPE samples from TFHL tissues were incubated in a dry oven for
322 15 min at 55°C, deparaffinized, and rehydrated using a graded ethanol series. Antigen retrieval
323 was performed using Target Retrieval Solution pH 9.0 (Dako) in a Decloaking Chamber
324 (Biocare Medical, Pacheco, CA, USA) for 10 min at 95°C. Slides were incubated overnight at
325 4°C with a cocktail of metal-conjugated primary antibodies after blocking with buffer
326 containing 3% BSA. The following day, slides were washed twice with Dulbecco's PBS and
327 counterstained using Cell-ID Intercalator-Ir (Standard BioTools Inc.) for 30 min at RT to
328 visualize the DNA. After a final wash in doubly distilled H₂O, the slides were air-dried for 20

329 min. IMC data was acquired using a Hyperion imaging system (Standard BioTools Inc.).
330 Subsequently, five regions of interest (ROIs) of $1\,500 \times 1\,500\ \mu\text{m}$ per 1 FFPE sample were
331 identified on consecutive Hematoxylin and Eosin (H&E)-stained slides and ablated by the laser
332 beam.

333 We converted raw data, exported as MCD files, to the OME-TIFF format and segmented
334 into single cells using the `ImcSegmentationPipeline` [39]. Specifically, we applied `Ilastik`
335 (v1.3.3) [40] for pixel classification and generated pixel probability maps for three labels
336 (“nucleus,” “cytoplasm,” and “background”). Then, cells were segmented based on pixel
337 probabilities and single-cell or image features, such as channel intensities and the number of
338 neighbors, were measured using the `CellProfiler` (v4.2.1) [41].

339 The output data from `CellProfiler` was imported into R (v4.1.0) as a `SpatialExperiment`
340 object by the `imcRtools` package (v1.0.2) [42]. After the inverse hyperbolic sine transformation
341 and normalization at the 99th percentile, batch effect correction and unsupervised clustering
342 were performed using the `Batchelor` and `Seurat` packages, like with the scRNA-seq data. When
343 performing clustering, four proteins with poor cell-to-cell variability (CD10, E-cadherin,
344 ICOSL, and CD40LG) and two proteins related to the stromal structures (α -smooth muscle
345 actin [SMA] and collagen type I) were excluded. By annotation with canonical markers, we
346 identified a T_{FH} marker-positive cluster thought to be tumor cells and performed re-clustering
347 with immune and stromal cells other than tumor cells. Next, we computed the averaged cell-cell
348 interaction counts and compared them to a null distribution of counts generated by random
349 permutations to estimate the interaction or avoidance between cell types using the
350 “`testInteractions`” function of `imcRtools` (Table S19). Finally, the pixel- and cell-level
351 visualization of each image was performed by the `cytomapper` package (v1.6.0) [43].

352

353 **Code Availability**

354 The code used for data analysis are available from the corresponding author upon request
355 (sakatama@md.tsukuba.ac.jp [M.S.-Y.]).

356

357 **Supplementary Notes**

358 **Supplementary Note 1: Related to “Expansion of dysfunctional CD8⁺ and regulatory T cells
359 in LNs” and “Clonal tracking between T cells in LNs and PB”**

360 The following is a comment regarding subclustering and the TCR analysis of non-malignant PB
361 T cells.

362 Subclustering of non-malignant PB T cells revealed a similar immunophenotype to those
363 of LNs. Specifically, the proportions of CD8 T_{DYS} and T_{PRO/DYS} were increased, whereas those of
364 CD4/CD8 T_N and T_{CM} were decreased in patients with TFHL compared with those in HDs (Fig.
365 S10A–B). Although the increase in the proportion of T_{REG} was not significant, the proportion of
366 proliferating T_{REG} and the expression levels of T_{REG} activation markers such as *FOXP3*, *BATF*,
367 *TNFRSF4*, and *TNFRSF18* [44] and co-inhibitory molecules such as *PDCDI* and *TIGIT* were
368 higher in the T_{REG} of patients with TFHL than those of HDs (Fig. S10C–F).

369 By TCR repertoire analysis of non-malignant T cells in PB, we found that effector CD8⁺
370 T cells (effector memory [T_{EM}] and effector memory cells re-expressing CD45RA [T_{ERMA}]) were
371 clonally expanded in both patients with TFHL and HDs, whereas CD8 T_{DYS}/T_{PRO/DYS} were
372 clonally expanded only in the patients with TFHL (Fig. S17A). TCR overlap analysis showed
373 that CD8 T_{DYS} and CD8 T_{PRO/DYS} shared their TCRs in TFHL PB while no shared TCRs were
374 detected between effector and dysfunctional CD8⁺ T cells of TFL PB, unlike the LN data (Fig.
375 S17B). In addition, over 50% of known, pathogen-specific CDR3s, such as cytomegalovirus

376 (CMV), Epstein-Barr virus (EBV), and influenza virus detected by collation with VDJdb
377 database [45], were concentrated in effector CD8⁺ T cells in both TFHL patients and HDs,
378 suggesting that they were “bystander” CD8⁺ T cells that recognized antigens unrelated to tumor
379 cells (data not shown).

380

381 **Supplementary Note 2: Related to “*In-silico* and spatial intercellular interactions and**
382 **formation of the TFHL immune-evasive microenvironment”**

383 The following is a comment regarding the subclustering and annotation of non-malignant cells
384 in the spatial analysis.

385 By unsupervised clustering and annotation using canonical markers, we identified 14
386 subclusters: granzyme B (GZMB)^{low} PD1^{high} CD8 T_{DYS}, GZMB^{high} PD1^{low} CD8 T_{EFF},
387 FOXP3/CD25⁺ T_{REG}, CD3/CD4⁺ or CD3/CD8⁺ T cells, CD19⁺ B cells, CD3⁻ CD4^{dim} CD14⁺
388 myeloid cells, CD3/CD4/CD19⁻ CD132/CD11B⁺ NK cells, and CD21/CD35⁺ follicular
389 dendritic cells (FDCs) (Table S18). Cluster 10 showed CD20⁻ CD19/CD79A^{dim}, annotated as
390 PBL/PC (Fig. S18A). Cluster 13 exhibited high expressions of α -SMA and collagen type I,
391 whereas lineage markers were negative (Fig. S18B), suggestive of stromal cells such as
392 endothelial cells of blood and lymphatic vessels.

393 Consistent with previous reports on AITL [46], FDCs formed meshwork structures and
394 were identified as indistinguishable clusters from surrounding cells (clusters 3, 6, and 11; Fig.
395 S18C). Moreover, B cells adjacent to tumor cells were recognized as a single cluster with tumor
396 cells (cluster 12; Fig. S18D).

397 **Supplementary Table Legends**

398 **Supplementary Table 1.** Characteristics of patients with TFHL and controls and comparison of
399 patient cohorts.

400 **Supplementary Table 2.** IMC analysis of TFHL tumor tissues.

401 **Supplementary Table 3.** Summary of tumor-cell clonotypes detected by scTCR-seq.

402 **Supplementary Table 4.** Proportion of cells detected by scRNA-seq and FCM analysis.

403 **Supplementary Table 5.** Somatic mutations detected by WES of 14 patients with TFHL.

404 **Supplementary Table 6.** Marker genes for each subcluster of LN and PB tumor cells.

405 **Supplementary Table 7.** Somatic mutations detected by reanalysis of scRNA-seq.

406 **Supplementary Table 8.** DEGs upregulated in LN and PB tumor cells compared with all
407 MNCs and normal T_{FH} cells.

408 **Supplementary Table 9.** DEG analysis of three candidate genes for novel tumor cell-specific
409 markers compared with all non-malignant MNCs.

410 **Supplementary Table 10.** IHC staining of PLS3 on PTCLs and B-cell lymphomas.

411 **Supplementary Table 11.** DEGs between T_{REG} of RR TFHL LNs and HLNs.

412 **Supplementary Table 12.** DEGs between *FCRL4*⁺ MBCs (B2) and *FCRL4*⁻ MBCs (B1) of
413 LNs.

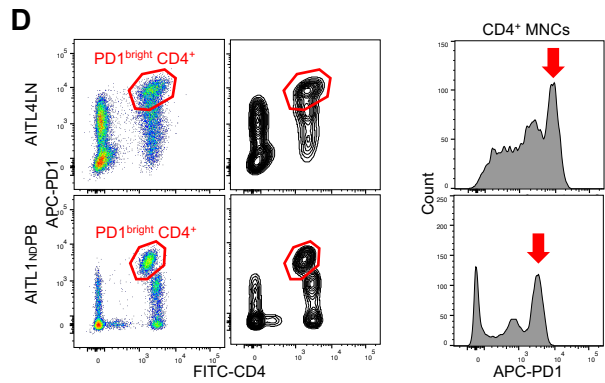
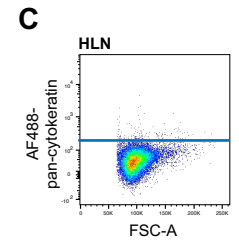
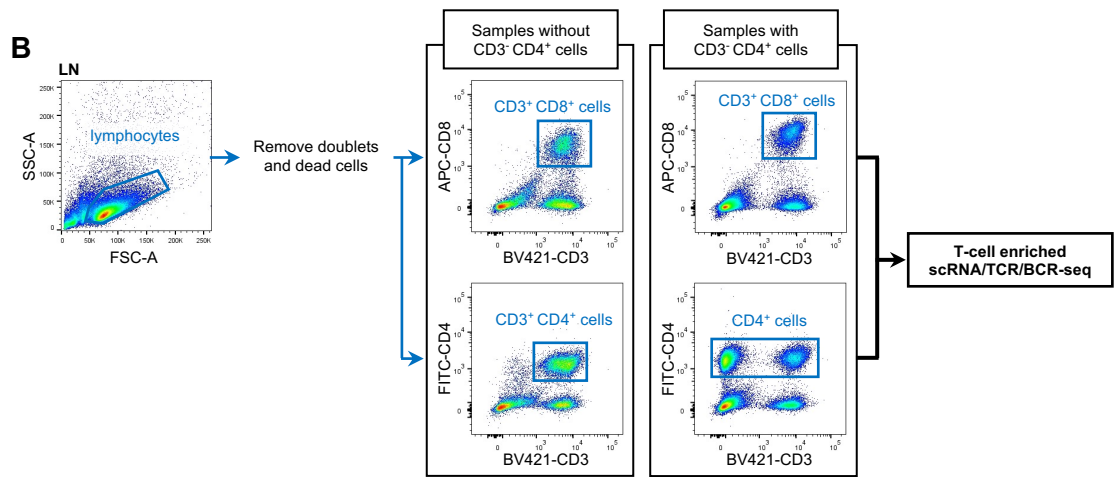
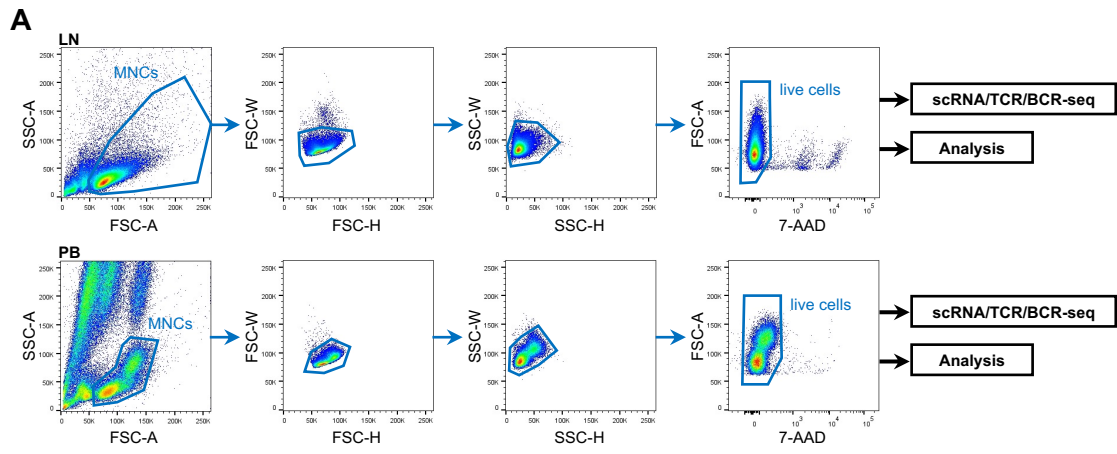
414 **Supplementary Table 13.** DEGs in *FCRL4*⁺ MBCs (B2) of ND or RR TFHL LNs compared
415 with those of HLNs.

416 **Supplementary Table 14.** AITL B-specific gene set cited from Fujisawa et al. (2022) [1] for
417 GSEA.

418 **Supplementary Table 15.** DEGs in *XCL1*⁺ NK cells (NK1) of ND TFHL LNs compared with
419 those of HLNs.

- 420 **Supplementary Table 16.** DEGs in *XCL1*⁺ NK cells (NK1) of RR TFHL LNs compared with
421 those of HLNs.
- 422 **Supplementary Table 17.** Antibodies used for IMC analysis.
- 423 **Supplementary Table 18.** Markers and annotation of each cluster for subclustering of non-
424 malignant cells in IMC analysis.
- 425 **Supplementary Table 19.** Results of spatial interaction analysis.
- 426 **Supplementary Table 20.** Antibodies used for FCM analysis and IHC staining.

Supplementary Figure 1



427 **Figure S1. Cell-surface protein expression analysis and sorting by flow cytometry (FCM)**

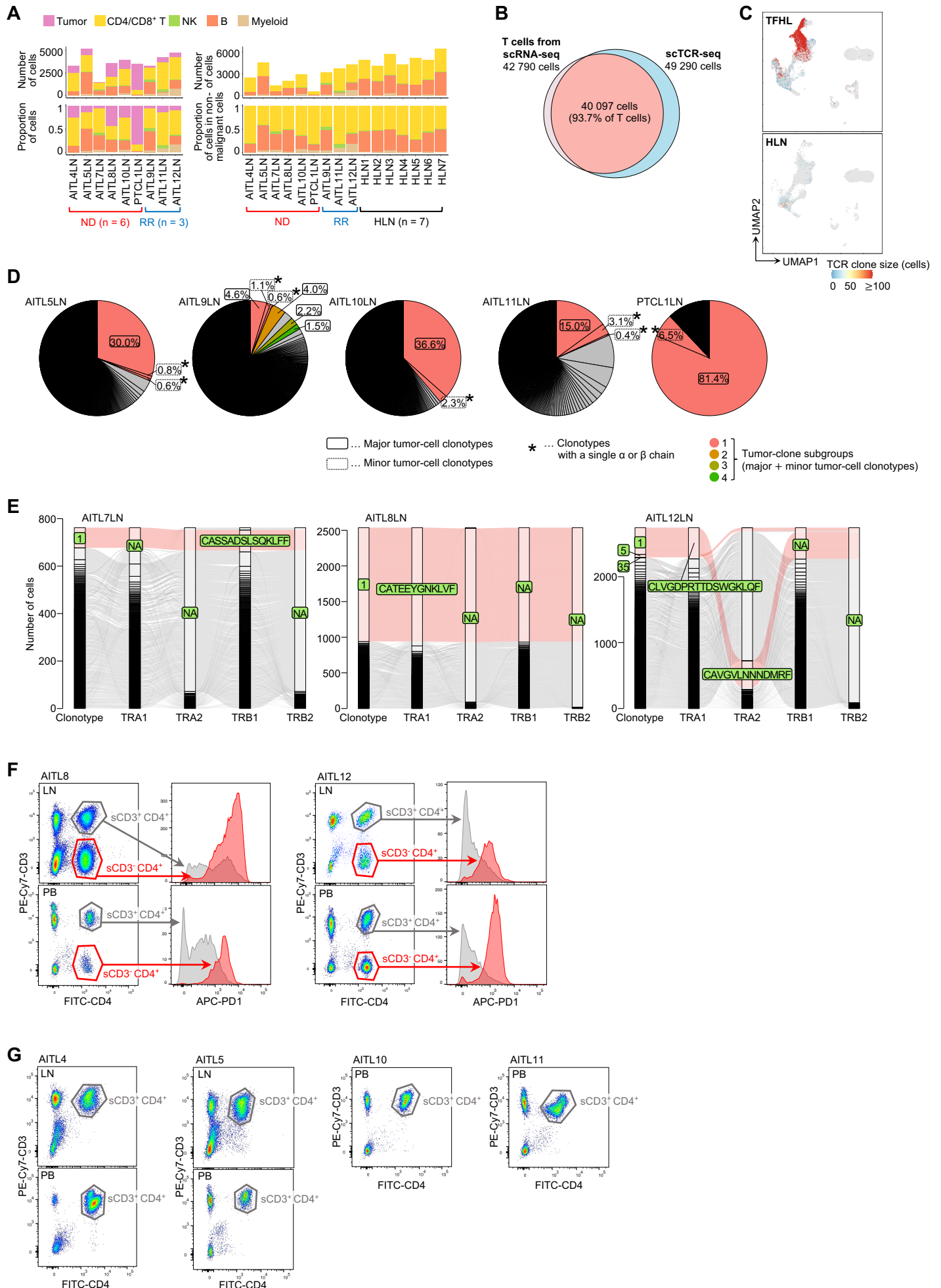
428 (A) Mononuclear cell (MNC) sorting of lymph node (LN) and peripheral blood (PB) samples.
429 After removing doublets and dead cells by forward versus side scatter plot and 7-Amino-
430 Actinomycin D (7-AAD) staining, MNCs were sorted, and library construction of single-cell
431 RNA and T-/B-cell receptor (TCR/BCR) sequencing (scRNA/TCR/BCR-seq) or FCM analysis
432 were performed. FSC, forward scatter; SSC, side scatter.

433 (B) CD4/CD8⁺ T-cell sorting for T cell-enriched library. For samples in which tumor-
434 containing CD3⁻CD4⁺ cells were detected in the lymphocyte fraction in the initial analysis, CD3⁺
435 CD8⁺ cells and CD4⁺ cells were sorted.

436 (C) Cytokeratin staining for homeostatic LNs (HLNs). Cytokeratin negativity confirmed the
437 absence of tumor-cell contamination.

438 (D) Detection of tumor cells by surface antigen. Tumor cells were detected as a PD1^{bright} CD4⁺
439 T-cell population, as previously reported [47].

Supplementary Figure 2



440 **Figure S2. Subclustering and TCR repertoire analysis of LN samples**

441 (A) Absolute number (top of panels) and proportion (bottom of panels) of cells within all LN
442 MNCs (left panel) and non-malignant LN MNCs (right panel) for each sample, color-coded by
443 cell types. B, B cell; CD4/CD8 T, CD4⁺ and CD8⁺ T cell; Myeloid, myeloid cell; NK, natural
444 killer cell; ND, newly diagnosed T follicular helper cell lymphoma (TFHL); RR, relapsed or
445 refractory TFHL; Tumor, tumor cell.

446 (B) Comparison between T cells from scRNA-seq data and TCRs from scTCR-seq data of LN
447 samples.

448 (C) Clone size of TCRs in LNs. The number of cells expressing each clonotype was defined
449 as clone size and illustrated for each cell.

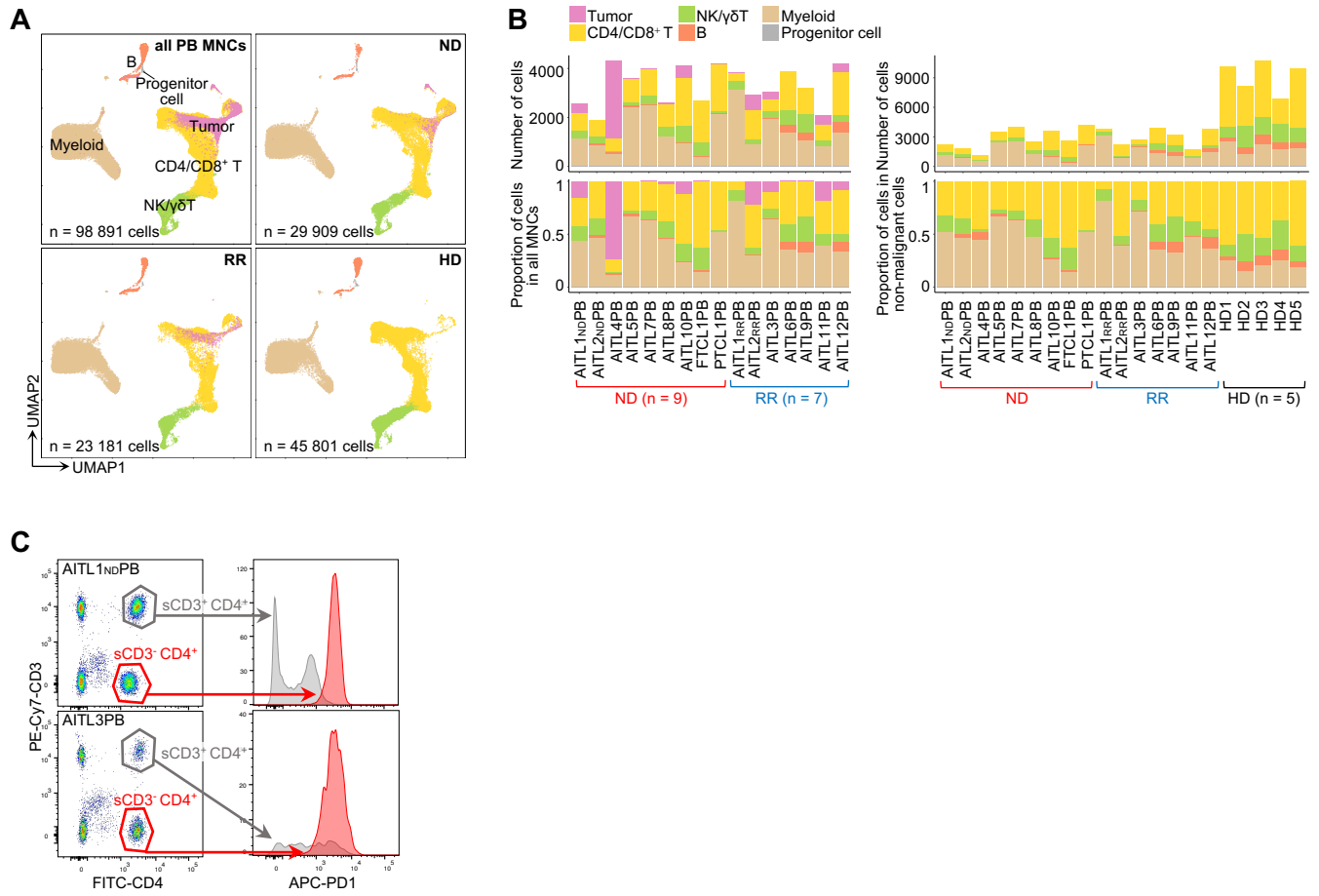
450 (D) Pie charts of TCR clonotypes for each sample. Tumor clones are colored.

451 (E) Sankey plots of each clonotype in cases where the major tumor-cell clonotype was a TCR
452 with a single chain. The major clonotypes are colored in red and green, showing the CDR3
453 sequences per TCR chain. "NA" indicates that no TCR chain was detected. NA, not available;
454 TRA, TCR alpha chain; TRB, TCR beta chain.

455 (F) Relationship between CD3⁻ CD4⁺ cells and the expression level of PD1 in each sample.
456 CD3⁻ CD4⁺ (red) and CD3⁺ CD4⁺ (grey) populations detected by a CD3 versus CD4 plot (left
457 panel) are plotted separately on a histogram of PD1 expression (right panel). Samples in which
458 CD3⁻ CD4⁺ cells were detected by FCM analysis of LN samples are shown. sCD3 ϵ , surface CD3 ϵ .

459 (G) FCM plots of CD3 versus CD4 for TFHL patients without single-chain TCR expansion.
460 Since LN samples from AITL10 and AITL11 were not available for detailed FCM analysis, only
461 PB FCM data are shown for these patients.

Supplementary Figure 3



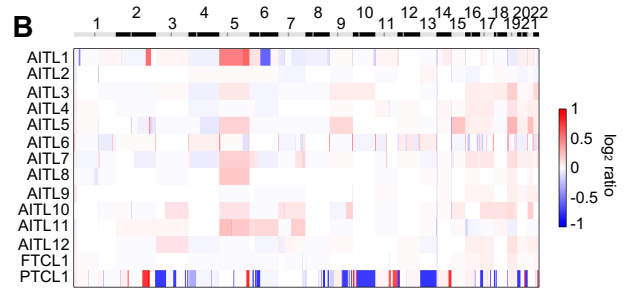
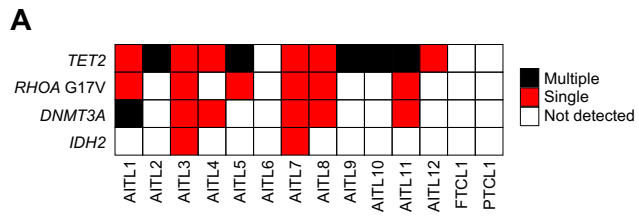
462 **Figure S3. Single-cell analysis of PB samples**

463 (A) Uniform Manifold Approximation and Projection for Dimension Reduction (UMAP) plots
464 of all PB MNCs from 16 TFHL and 5 healthy donor (HD) PB samples, colored according to cell
465 type (top left). Cells are shown separately for each clinical status (top right and bottom). NK/ $\gamma\delta$ T,
466 natural-killer and gamma-delta T cell.

467 (B) Absolute number (top of panels) and proportion (bottom of panels) of cells within all PB
468 MNCs (left panel) and non-malignant PB MNCs (right panel) for each sample, color-coded by
469 cell types.

470 (C) Relationship between CD3⁻ CD4⁺ cells and the expression level of PD1 in PB samples.
471 CD3⁻ CD4⁺ (red) and CD3⁺ CD4⁺ (grey) populations detected by a CD3 versus CD4 plot (left
472 panel) are plotted separately on a histogram of PD1 expression (right panel). Samples in which
473 CD3⁻ CD4⁺ cells were detected by FCM analysis of PB samples are shown.

Supplementary Figure 4

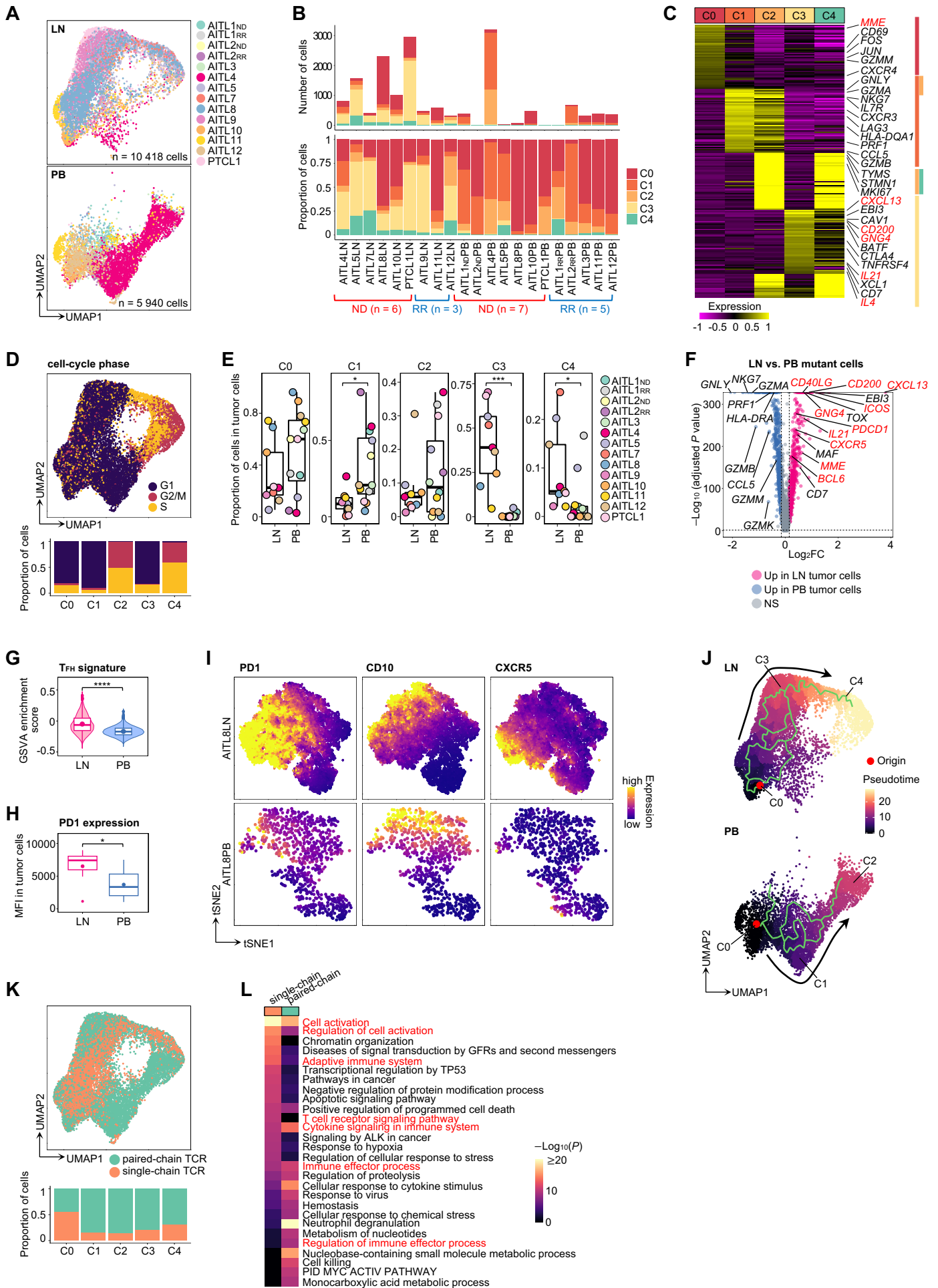


474 **Figure S4. Bulk genomic profiling of the 14 TFHL patients**

475 (A) Recurrent gene mutations detected by whole-exome sequencing (WES). Red squares
476 indicate single mutations and black ones indicate multiple mutations.

477 (B) Copy number variation (CNV) analysis using WES data from tumor tissue samples.
478 Significant CNVs were called by the Genome Analysis Tool Kit [34].

Supplementary Figure 5



479 **Figure S5. Subclustering of tumor cells from LN and PB samples**

480 (A) UMAP plots of LN and PB tumor cell subclusters. Cells are color-coded by each sample
481 and shown separately for each tissue.

482 (B) Absolute number (top) and proportion within all tumor cells (bottom) of cells for each
483 sample, color-coded by tumor subclusters.

484 (C) Heatmap of the top 50 differentially expressed genes (DEGs) for each subcluster. T
485 follicular helper (T_{FH}) markers are shown in red.

486 (D) Feature plot showing estimation of cell cycle phase. Cell cycle score calculations were
487 performed based on canonical markers using the “CellCycleScoring” function of Seurat, and each
488 cell is colored according to the estimated cell cycle phase.

489 (E) Comparison of the proportion of each cluster in LN and PB tumor cells. The boxplots show
490 the median (center line), interquartile range (box limits), minimum to max values (whiskers), and
491 samples (dots) for each group. *P*-values are shown only when there is a significant difference.

492 (F) Volcano plot of DEGs between LN (pink) and PB (blue) tumor cells. NS, not significant;
493 vs., versus.

494 (G) Comparison of gene set variation analysis (GSVA) enrichment score for T_{FH} signature in
495 LN (pink) and PB (blue) tumor cells. The boxplots show the median (center line), mean (center
496 dot), interquartile range (box limits), and minimum to max values (whiskers) for each group.

497 (H) Comparison of PD1 expression levels by FCM in LN (pink) and PB (blue) tumor cells.
498 Tumor cells were detected as a $PD1^{bright} CD4^{+}$ T cell population by FCM [47]. The boxplots show
499 the median (center line), mean (center dot), interquartile range (box limits), and minimum to max
500 values (whiskers) for each group. MFI, median fluorescence intensity.

501 (I) t-Distributed Stochastic Neighbor Embedding (t-SNE) plots of FCM analysis for tumor
502 cells of AITL&LN (top) and AITL&PB (bottom), colored by the expression levels of T_{FH} markers

503 (PD1, CD10, and CXCR5).

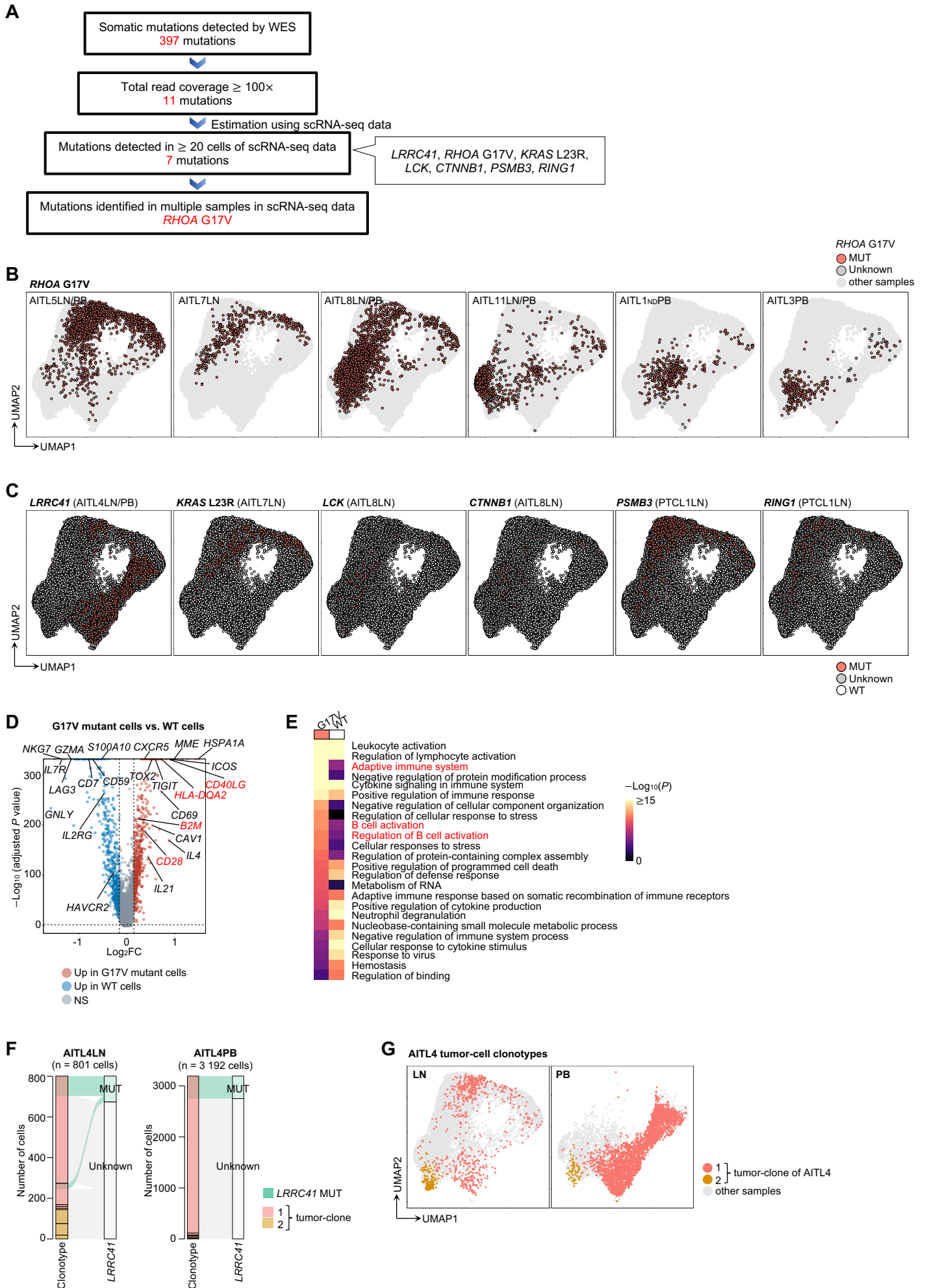
504 (J) Trajectory analysis by Monocle3 [27] for LN (top) and PB (bottom) tumor cells. The red
505 points were set as the origins of trajectory.

506 (K) UMAP plot showing tumor cells with paired-chain (green) and single-chain (orange) TCRs
507 (top) and their proportions in each cluster (bottom).

508 (L) Heatmap of gene ontology (GO) analysis of tumor cells with paired-chain (green) and
509 single-chain (orange) TCRs.

510 $*P < 5.0 \times 10^{-2}$, $***P < 1.0 \times 10^{-3}$, $****P < 1.0 \times 10^{-4}$.

Supplementary Figure 6



511 **Figure S6. Estimation of genetic mutations using single-cell data**

512 (A) Overview of reanalysis of somatic mutations using scRNA-seq data.

513 (B) Distribution of *RHOA* G17V (G17V) for each sample in LN and PB tumor cells. MUT,
514 mutant cells; Unknown, cells with no mutant reads or no coverage.

515 (C) Distribution of detectable mutations other than G17V (*LRRC41*, *KRAS* L23R, *LCK*,
516 *CTNNB1*, *PSMB3*, and *RING*) in LN and PB tumor cells. The sample names in parentheses show
517 the samples in which the mutations were detected. WT, wild-type cells.

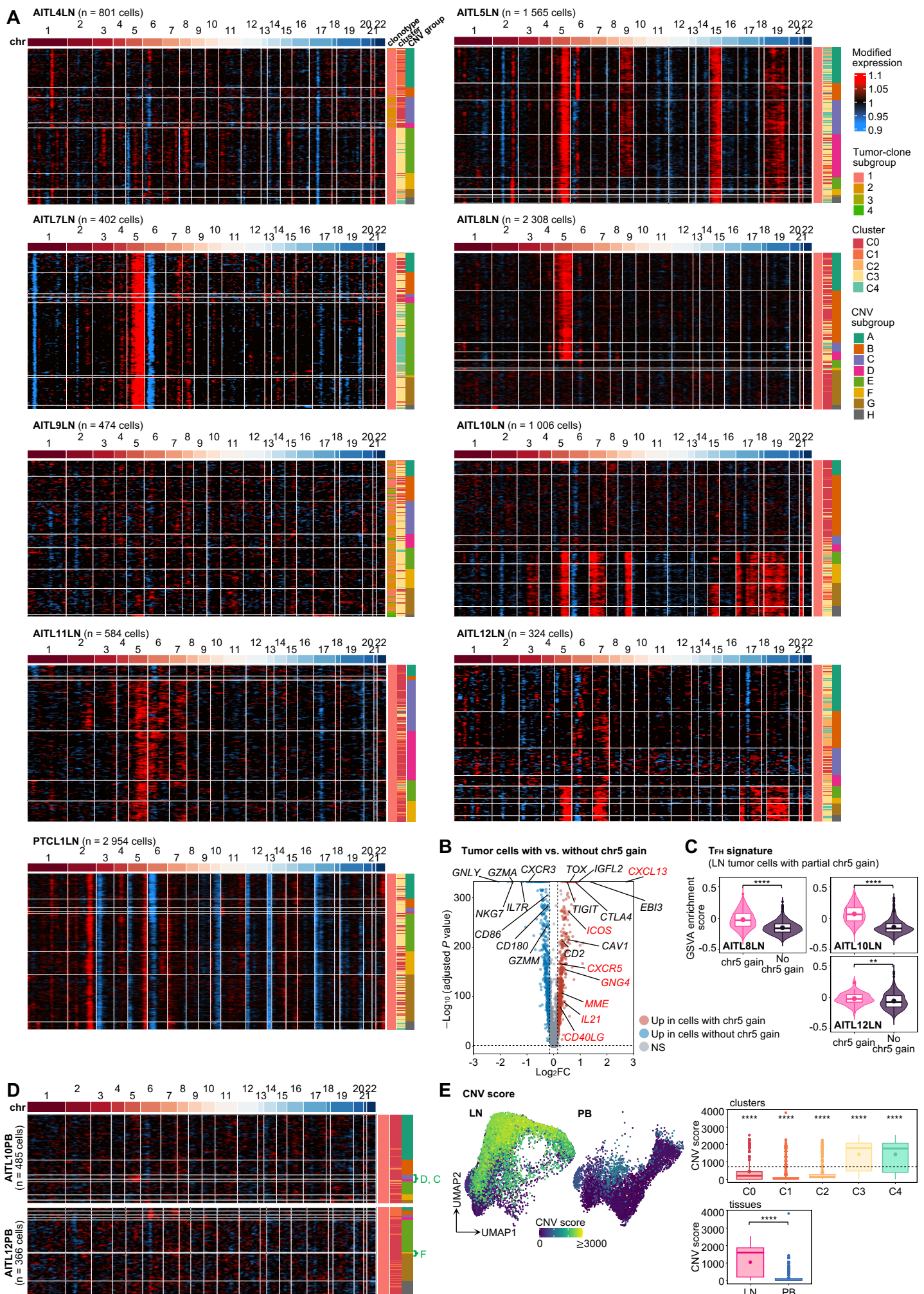
518 (D) Volcano plot of DEGs between G17V mutant (red) and WT (blue) cells in LN and PB
519 tumor cells. G17V unknown cells were removed from the analysis.

520 (E) Heatmap of GO analysis of G17V mutant (red) and WT (white) tumor cells.

521 (F) Relationship between *LRRC41* mutant cells and their clonotypes in AITL4LN/PB tumor
522 cells. In the Sankey plot, tumor clones of AITL4 and *LRRC41* mutant cells (green) are colored.

523 (G) UMAP plot showing the distribution of AITL4 tumor clones.

Supplementary Figure 7



524 **Figure S7. Inferring CNVs using single-cell data**

525 (A) Heatmaps of estimated CNVs for LN tumor cells by inferCNV [36]. Right bars represent
526 tumor clones, subclusters of tumor cells, and subgroups based on CNV patterns, respectively. chr,
527 chromosome.

528 (B) Volcano plot of DEGs between tumor cells with chr5 gain (red) and those without (blue).

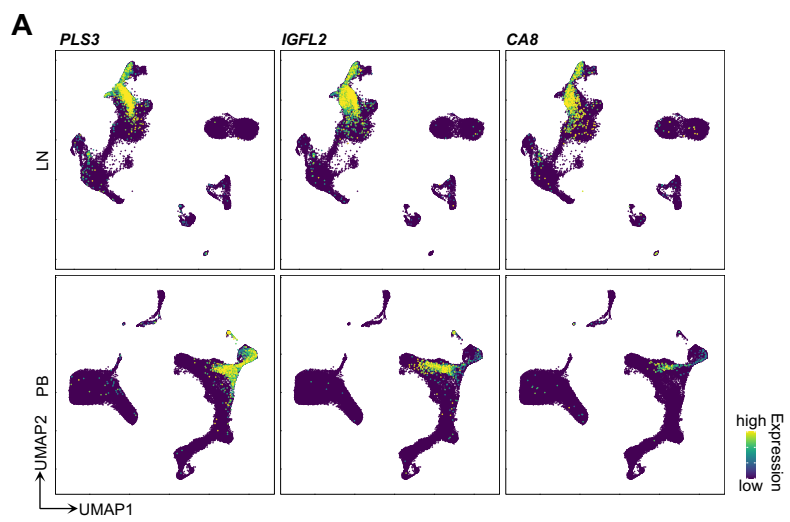
529 (C) Comparison of GSVA enrichment score for the T_{FH} signature between tumor cells with
530 chr5 gain (pink) and those without (blue) in TFHL LNs with partial chr5 gain.

531 (D) Heatmaps of estimated CNVs for PB tumor cells in AITL10 and AITL12.

532 (E) Distribution (left) and comparison for each cluster (top right) or tissue (bottom right) of
533 CNV scores estimated using scRNA-seq data. In the boxplots of the top right panel, the dotted
534 line represents the mean CNV scores across all clusters and adjusted *P*-values are calculated by
535 the pairwise Wilcoxon test for each cluster against the mean value of all clusters.

536 All boxplots show the median (center line), mean (center dot), interquartile range (box limits),
537 and minimum to max values (whiskers) for each group. ***P* < 1.0 × 10⁻², *****P* < 1.0 × 10⁻⁴.

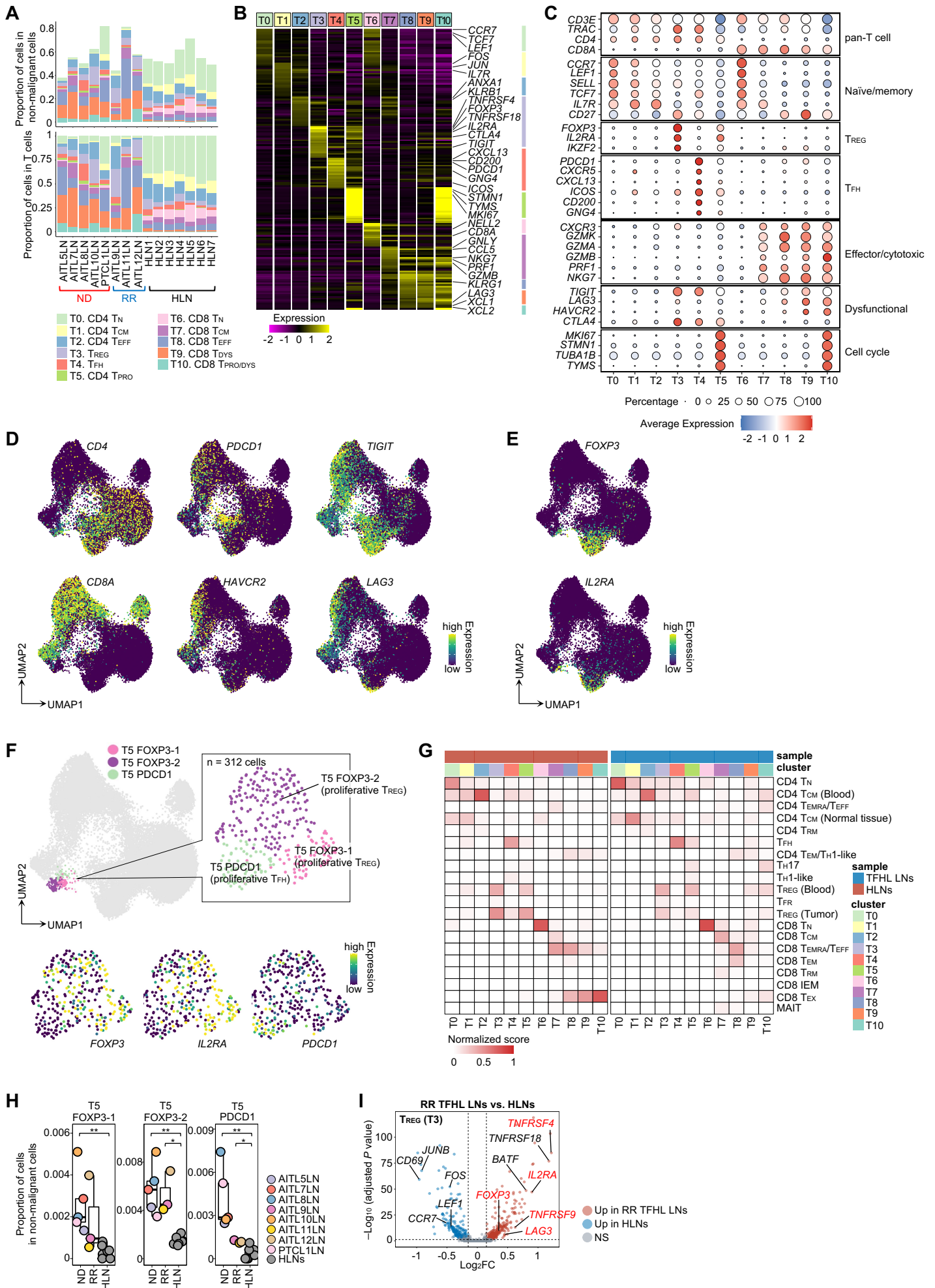
Supplementary Figure 8



538 **Figure S8. Identification of novel tumor-specific cell markers**

539 (A) Feature plots of candidate marker genes in all LN (top) and PB (bottom) MNCs.

Supplementary Figure 9



540 **Figure S9. Annotation of subclusters of non-malignant LN T cells**

541 (A) Proportion of each cluster within non-malignant MNCs (top) and within non-malignant T
542 cells (bottom) for each sample. T_{CM}, central memory T cell; T_{DYS}, dysfunctional T cell; T_{EFF},
543 effector T cell; T_N, naïve T cell; T_{PRO}, proliferative T cell; T_{PRO/DYS}, proliferative dysfunctional T
544 cell; T_{REG}, regulatory T cell.

545 (B) Heatmap of the top 20 DEGs for each cluster of non-malignant LN T cells.

546 (C) Average expression per cluster of selected markers for cell-type annotation in non-
547 malignant LN T cells.

548 (D) Feature plots of dysfunctional T-cell markers.

549 (E) Feature plots of T_{REG} markers.

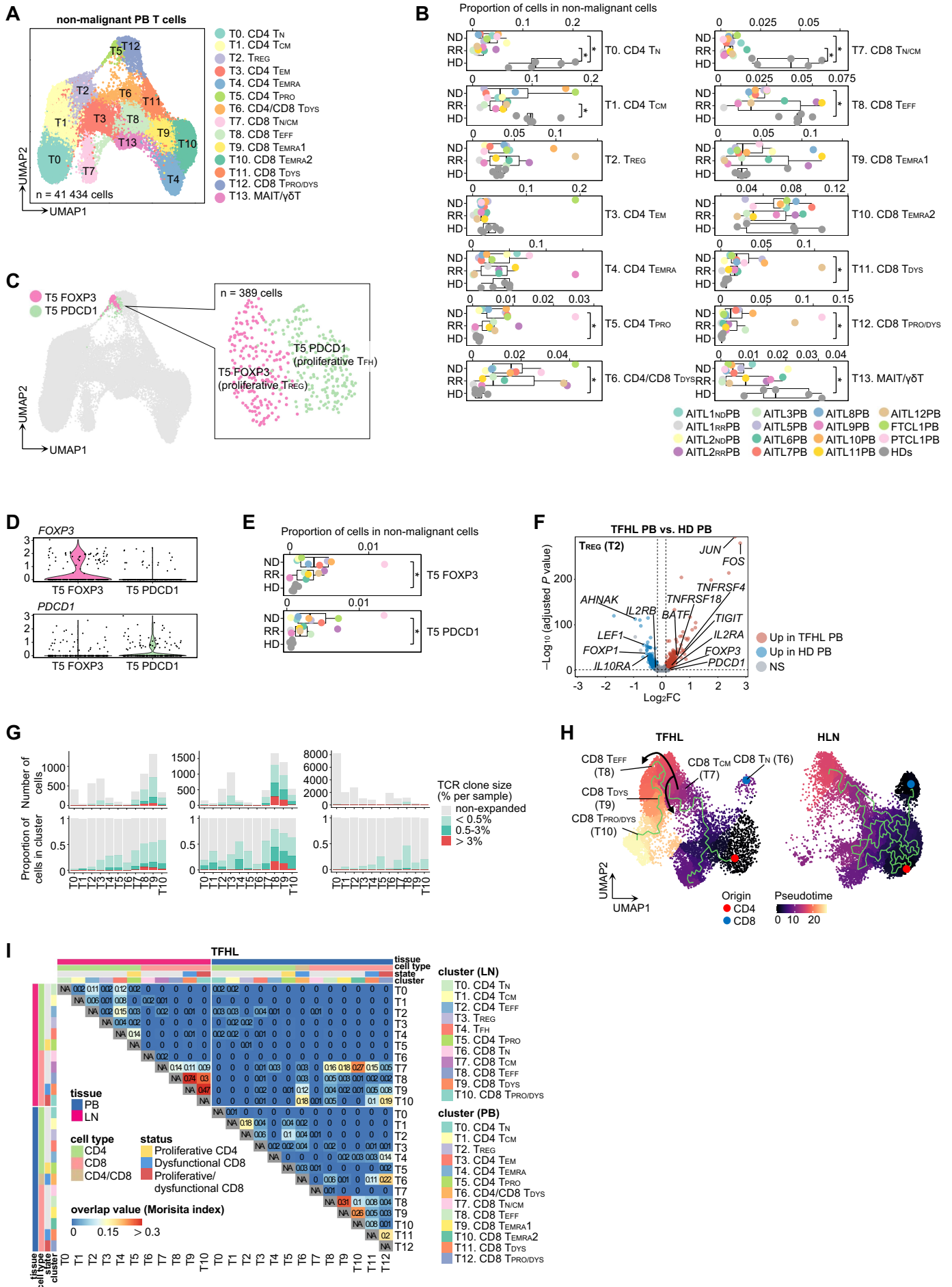
550 (F) Subclustering of the CD4 T_{PRO} (T5) cluster. UMAP plot (top) and feature plots of T_{REG} and
551 T_{FH} markers (bottom).

552 (G) Cell-type estimation scores by SingleR [13] using previously published single-cell data as
553 a reference [48] for each subcluster of non-malignant T cells.

554 (H) Comparison of proportions of each subcluster of CD4 T_{PRO} in non-malignant MNCs of
555 each sample. The boxplots show the median (center line), interquartile range (box limits),
556 minimum to max values (whiskers), and samples (dots) for each group. *P*-values are shown only
557 for significant differences. **P* < 5.0 × 10⁻², ***P* < 1.0 × 10⁻².

558 (I) Volcano plot of DEGs in T_{REG} from RR TFHL LNs (red) and those from HLNs (blue).

Supplementary Figure 10



559 **Figure S10. Subclustering of non-malignant PB T cells and non-malignant TCR repertoire**
560 **analysis**

561 (A) UMAP plot of non-malignant PB T-cell subclusters. MAIT/ $\gamma\delta$ T, mixture of mucosal-
562 associated invariant T cells and gamma-delta T cells; T_{EM}, effector memory T cell; T_{EMRA}, effector
563 memory T cells re-expressing CD45RA; T_{N/CM}, mixture of naïve T cells and memory T cells.

564 (B) Comparison of proportions of each cluster in non-malignant MNCs of each sample. *P*-
565 values are shown only for significant differences.

566 (C,D) Subclustering of CD4 T_{PRO} (T5) cluster from non-malignant PB T cells. UMAP plot (C)
567 and expression levels of *FOXP3* and *PDCDI* (D).

568 (E) Comparison of proportions of each T5 subcluster in non-malignant MNCs of each sample.
569 *P*-values are shown only for significant differences.

570 (F) Volcano plot of DEGs between PB T_{REG} of TFHL patients and those of HDs.

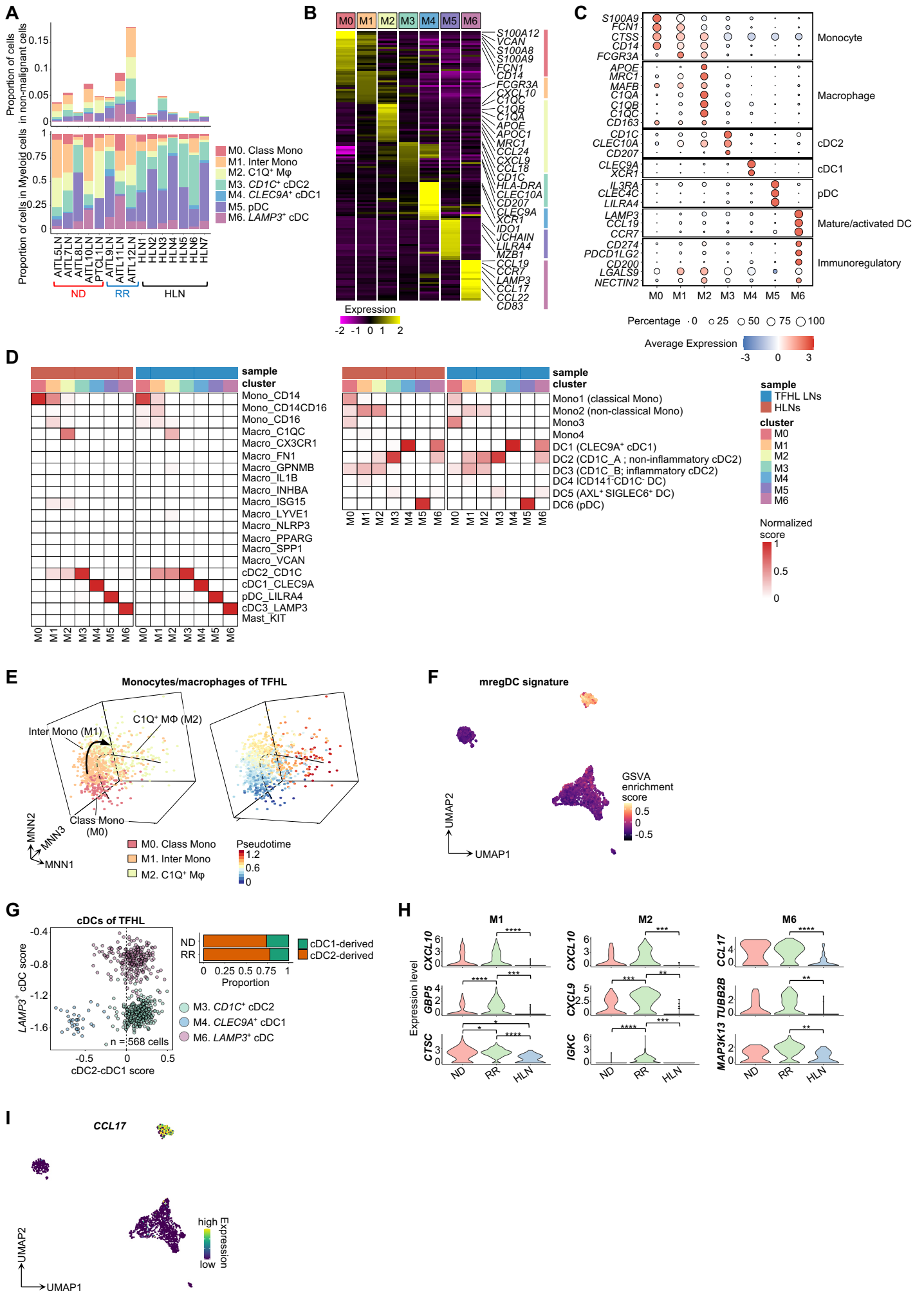
571 (G) Clone size of TCRs in non-malignant LN T cells. The proportion of each clonotype in all
572 TCRs of non-malignant T cells was calculated for each sample and shown separately for each
573 cluster. Non-expanded, clonotypes were expressed in < 2 cells.

574 (H) Trajectory analysis by Monocle3 [27] for non-malignant LN T cells. The red and blue
575 points were set as the origin of CD4⁺ and CD8⁺ T cells, respectively.

576 (I) TCR overlap analysis between LN (pink) and PB (blue) non-malignant T cells of TFHL
577 patients.

578 All boxplots show the median (center line), interquartile range (box limits), minimum to max
579 values (whiskers), and samples (dots) for each group. **P* < 5.0 × 10⁻².

Supplementary Figure 11



580 **Figure S11. Annotation of LN myeloid-cell subclusters**

581 (A) Proportions of each LN myeloid-cell subcluster within non-malignant MNCs (top) and
582 myeloid cells (bottom) for each sample. C1Q⁺ Mφ, complement component C1q positive
583 macrophage; CD1C⁺ cDC2, CD1C-positive type2 conventional dendritic cell; Class Mono,
584 classical monocyte; *CLEC9A*⁺ cDC1, *CLEC9A*-positive type1 cDC; Inter Mono, intermediate
585 monocyte; *LAMP3*⁺ cDC, *LAMP3*-positive cDC; pDC, plasmacytoid DC.

586 (B) Heatmap of the top 20 DEGs for each cluster of LN myeloid cells.

587 (C) Average expression per cluster of selected markers for cell-type annotation in LN myeloid
588 cells.

589 (D) Cell-type estimation scores by SingleR [13] for each cluster of LN myeloid cells using
590 scRNA-seq data from Cheng et al. [9] (left) and Villani et al. [5] (right).

591 (E) Trajectory inference by Slingshot [28] for LN monocytes and macrophages (M0–2) of
592 TFHL, color-coded by cluster (left) and pseudo-time (right).

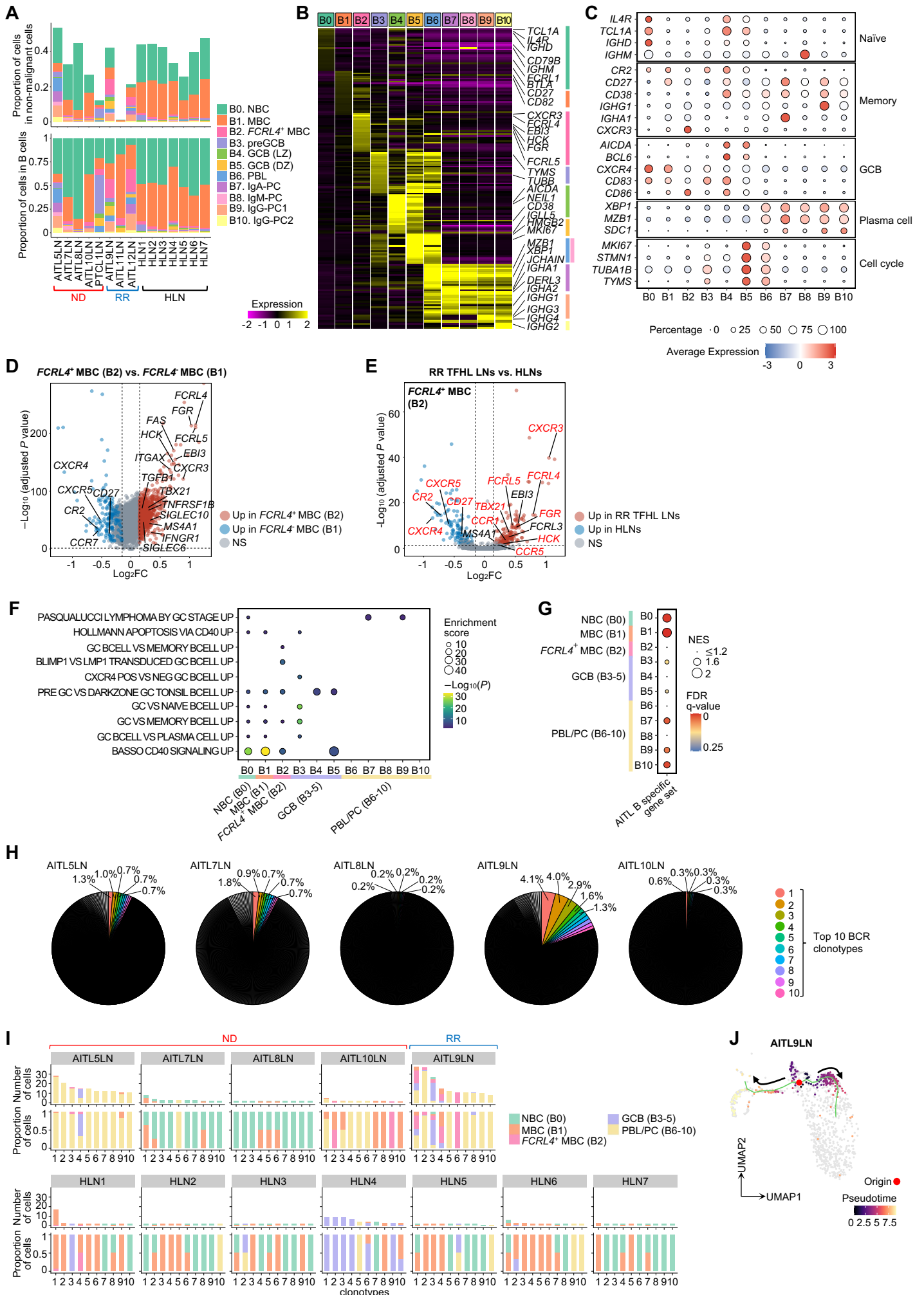
593 (F) GSVA enrichment scores for “mature DC enriched in immunoregulatory molecules
594 (mregDC)” signature [49] in LN myeloid cells.

595 (G) Estimation of the origin of *LAMP3*⁺ cDCs of TFHL using a previously reported scoring
596 system [9,49].

597 (H) Violin plots of the top 3 DEGs upregulated in myeloid subclusters increasing in RR TFHL
598 LNs compared with those of HLNs. *P*-values are shown only for significant differences. **P* < 5.0
599 × 10⁻², ***P* < 1.0 × 10⁻², ****P* < 1.0 × 10⁻³, *****P* < 1.0 × 10⁻⁴.

600 (I) Feature plot of *CCL17* in LN myeloid cells from TFHL patients.

Supplementary Figure 12



601 **Figure S12. Annotation of LN B-cell subclusters**

602 (A) Proportions of each LN B-cell subcluster within non-malignant MNCs (top) and within B
603 cells (bottom) for each sample. *FCRL4*⁺ MBC, *FCRL4*-positive memory B cell; GCB (DZ),
604 germinal center B cell in the dark zone; GCB (LZ), GCB in the light zone; MBC, memory B cell;
605 NBC, naïve B cell; PBL, plasmablast; PC, plasma cell; preGCB, pre-germinal center B cell.

606 (B) Heatmap of the top 25 DEGs for each cluster of LN B cells.

607 (C) Average expression per cluster of selected markers for cell-type annotation in LN B cells.

608 (D) Volcano plot of DEGs in *FCRL4*⁺ MBCs (B2, red) and *FCRL4*⁻ MBCs (B1, blue) of LNs.

609 (E) Volcano plot of DEGs in *FCRL4*⁺ MBCs from RR TFHL LNs (red) and those from HLNs
610 (blue).

611 (F) Dot plot of GO analysis of DEGs upregulated in B cells from TFHL LNs compared with
612 those from HLNs for GCB-related pathways analyzed by Fujisawa et al. [1].

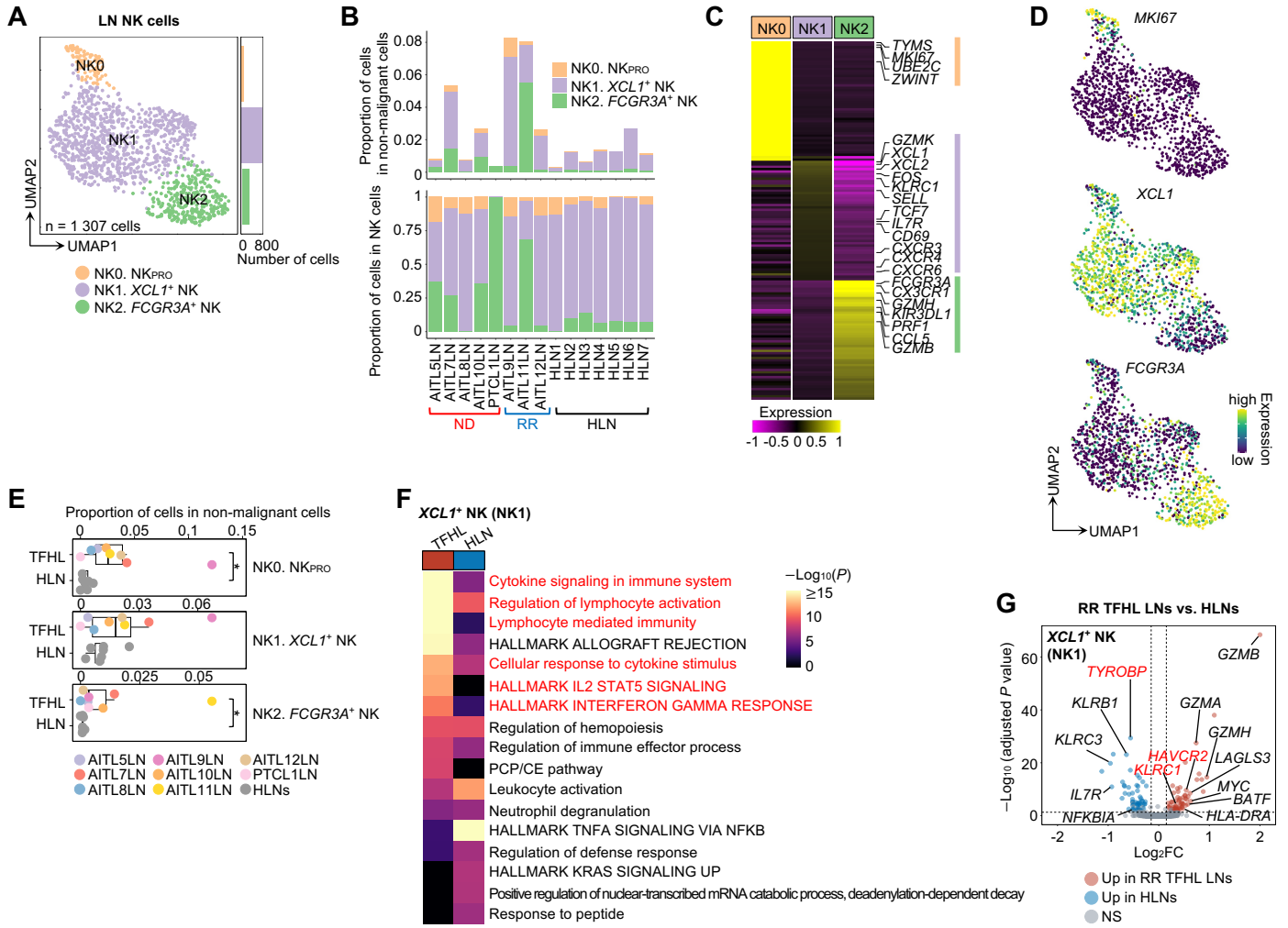
613 (G) Dot plot of gene set enrichment analysis for an AITL B-specific gene set previously
614 reported [1]. Cut-off, false discovery rate (FDR) q -value < 0.25; NSE, normalized enrichment
615 score.

616 (H) Pie charts of BCR clonotypes for each TFHL sample. The top 10 BCRs are colored and
617 the proportions of the top 5 BCRs are shown.

618 (I) Clone sizes of the top 10 BCR clonotypes for each LN sample. The number (top) and
619 proportions (bottom) of cells expressing each clonotype were shown color-coded by cell types.

620 (J) Trajectory analysis by Monocle3 [27] for the cells sharing BCRs with *FCRL4*⁺ MBCs in
621 AITL9LN. The red point was set as the origin of the trajectory. The cells without sharing the
622 BCRs are shown in gray.

Supplementary Figure 13



623 **Figure S13. Subclustering of LN NK cells**

624 (A) UMAP plot of LN NK-cell subclusters. *FCGR3A*⁺ NK, *FCGR3A*-positive activated natural
625 killer cell; NK_{PRO}, proliferative NK; *XCLI*⁺ NK, *XCLI*-positive tissue-resident NK.

626 (B) Proportions of each LN NK-cell subcluster within non-malignant MNCs (top) and within
627 NK cells (bottom) for each sample.

628 (C) Heatmap of the top 50 DEGs for each cluster of LN NK cells.

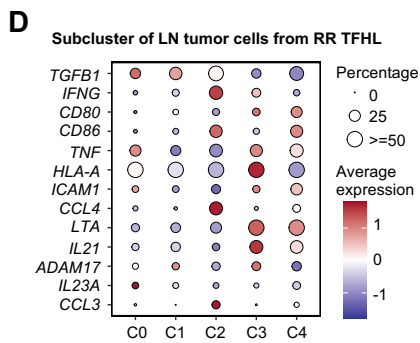
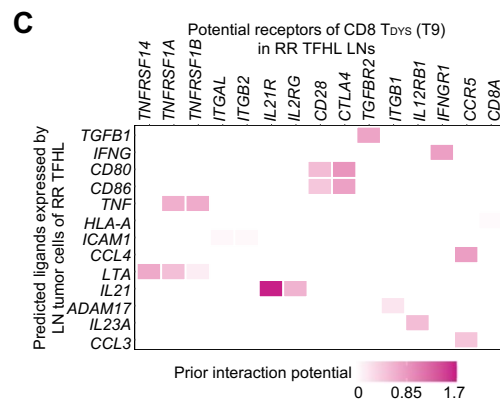
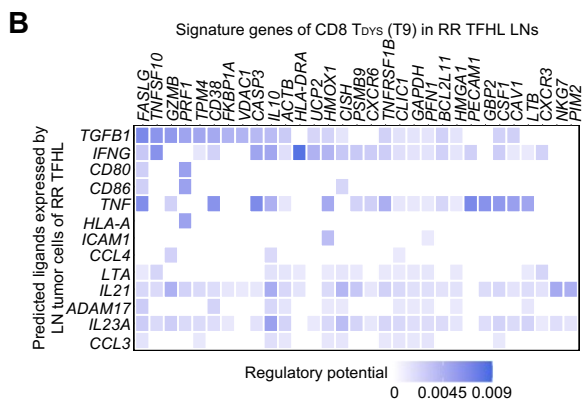
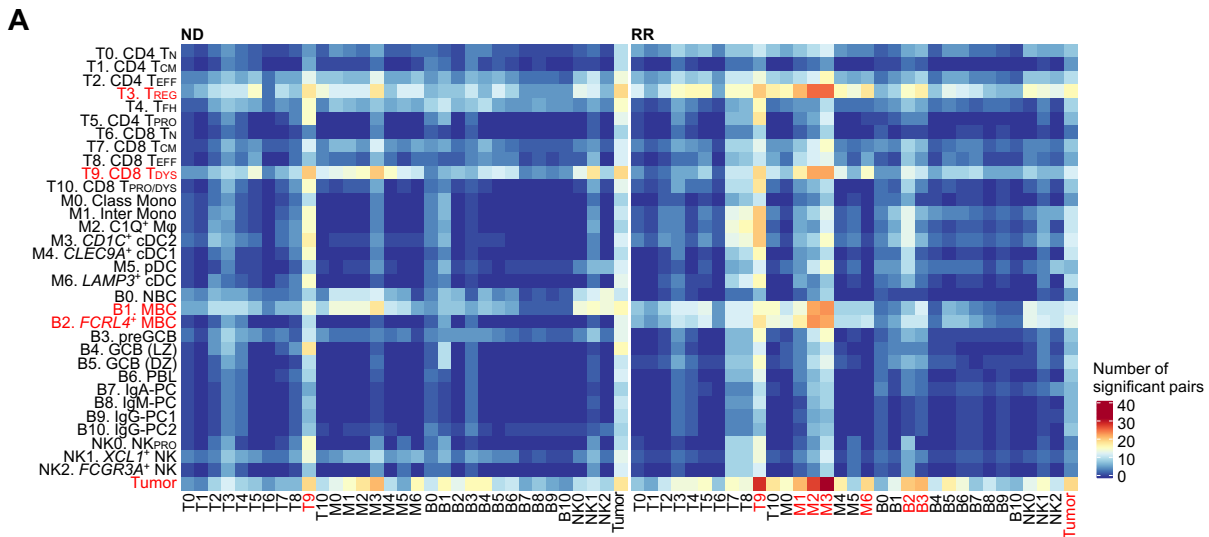
629 (D) Feature plots of marker genes in LN NK cells.

630 (E) Comparison of proportions of each subcluster of LN NK cells in non-malignant MNCs of
631 each sample. The boxplots show the median (center line), interquartile range (box limits),
632 minimum to max values (whiskers), and samples (dots) for each group. *P*-values are shown only
633 when there is a significant difference. **P* < 5.0 × 10⁻².

634 (F) Heatmap of the top 10 pathways detected by GO analysis between *XCLI*⁺ NKs (NK1) from
635 TFHL LNs and those from HLNs.

636 (G) Volcano plot of DEGs in *XCLI*⁺ NKs (NK1) from RR TFHL LNs (red) and those from
637 HLNs (blue).

Supplementary Figure 14



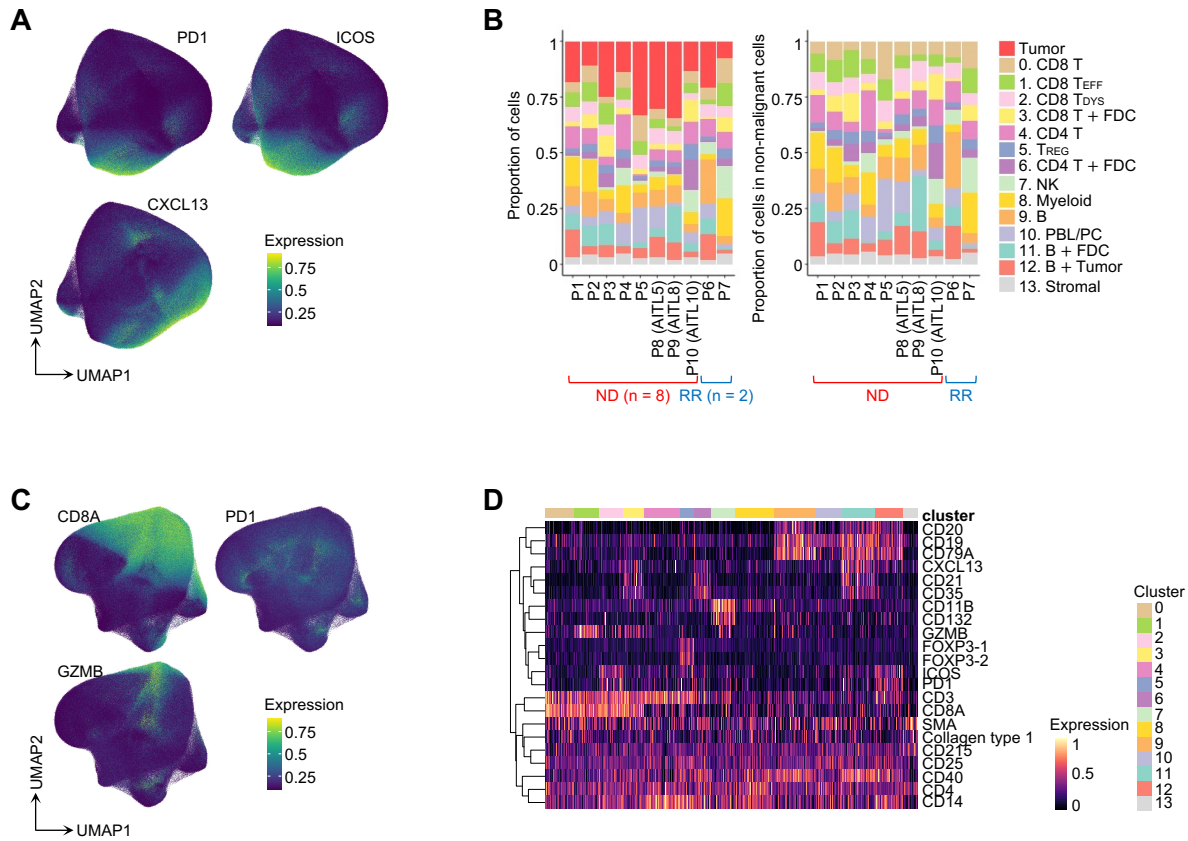
638 **Figure S14. *In silico* cell-cell interaction analysis of TFHL LNs**

639 (A) Number of significant interactions detected by *in silico* cellular interaction analysis using
640 CellPhoneDB [29] performed between tumor cells and subclusters of immune cells from ND (left)
641 and RR (right) TFHL LNs.

642 (B,C) Estimation of possible ligands (B), which can cause dysfunctional/exhausted signatures
643 of CD8 T_{DYS} from RR TFHL LNs, and their receptors expressed on tumor cells (C) by NicheNetR
644 [30]. Only interactions selected based on validated curated ligand-receptor databases are
645 visualized.

646 (D) Dot plot of average expression per tumor-cell subcluster of the receptors that can drive the
647 CD8 T_{DYS} signature estimated by NicheNetR.

Supplementary Figure 15



648 **Figure S15. Single-cell spatial analysis of TFHL tissues**

649 (A) Feature plots of T_{FH} markers in all cells from TFHL tissues.

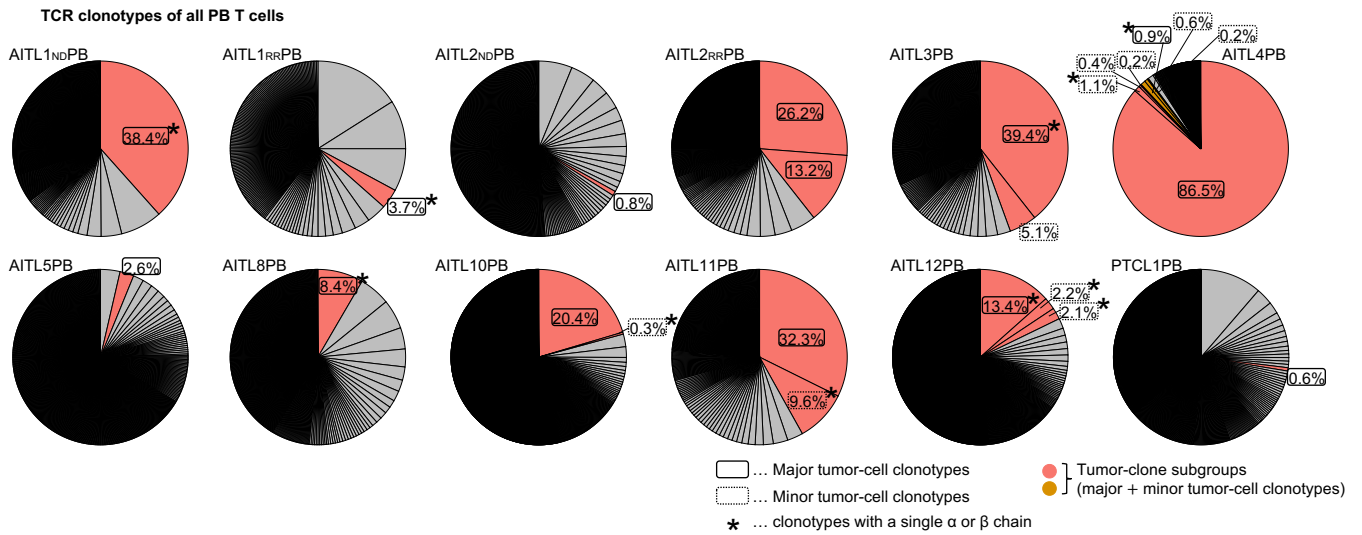
650 (B) Proportions of each cluster within all cells (left) and within non-malignant cells (right) for
651 each sample.

652 (C) Feature plots of markers related to $CD8^+$ T cell types in non-malignant cells.

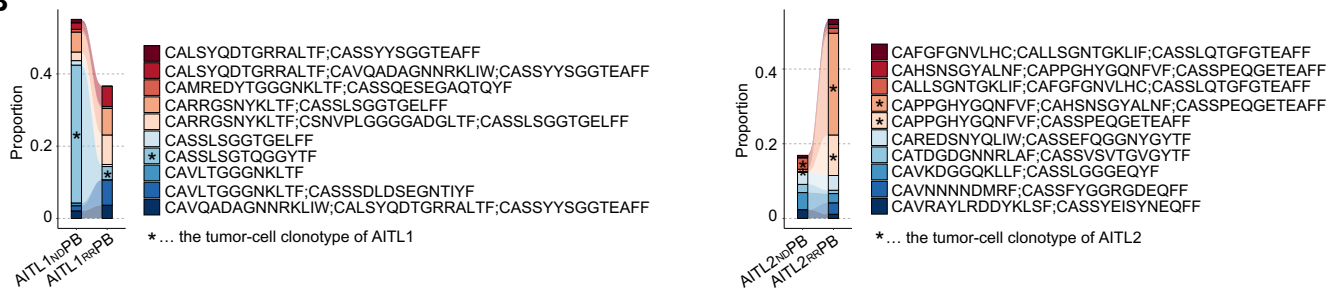
653 (D) Heatmap of markers for each cluster of non-malignant cells.

Supplementary Figure 16

A



B

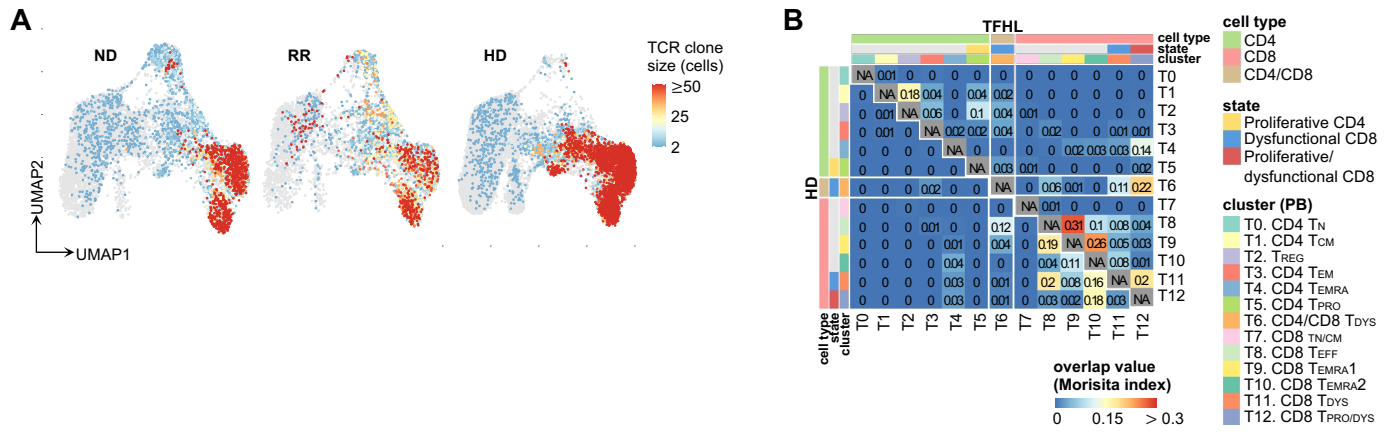


654 **Figure S16. TCR repertoire analysis of PB samples**

655 (A) Pie charts of TCR clonotypes for each sample. Tumor clones are colored. Major tumor-
656 cell clonotypes are indicated by solid lines, and minor tumor-cell clonotypes are indicated by
657 dotted lines. Clonotypes with only one TCR chain are indicated by an asterisk (*).

658 (B) Sankey plots showing TCR tracking of sequential samples (AITL1 and AITL2). The top
659 10 clonotypes of samples from ND (AITL1_{ND} and AITL2_{ND}) and RR (AITL1_{RR} and AITL2_{RR})
660 TFHLs were compared and CDR3 sequences of each clonotype are shown. The major clonotypes
661 of tumor cells are indicated by an asterisk (*).

Supplementary Figure 17

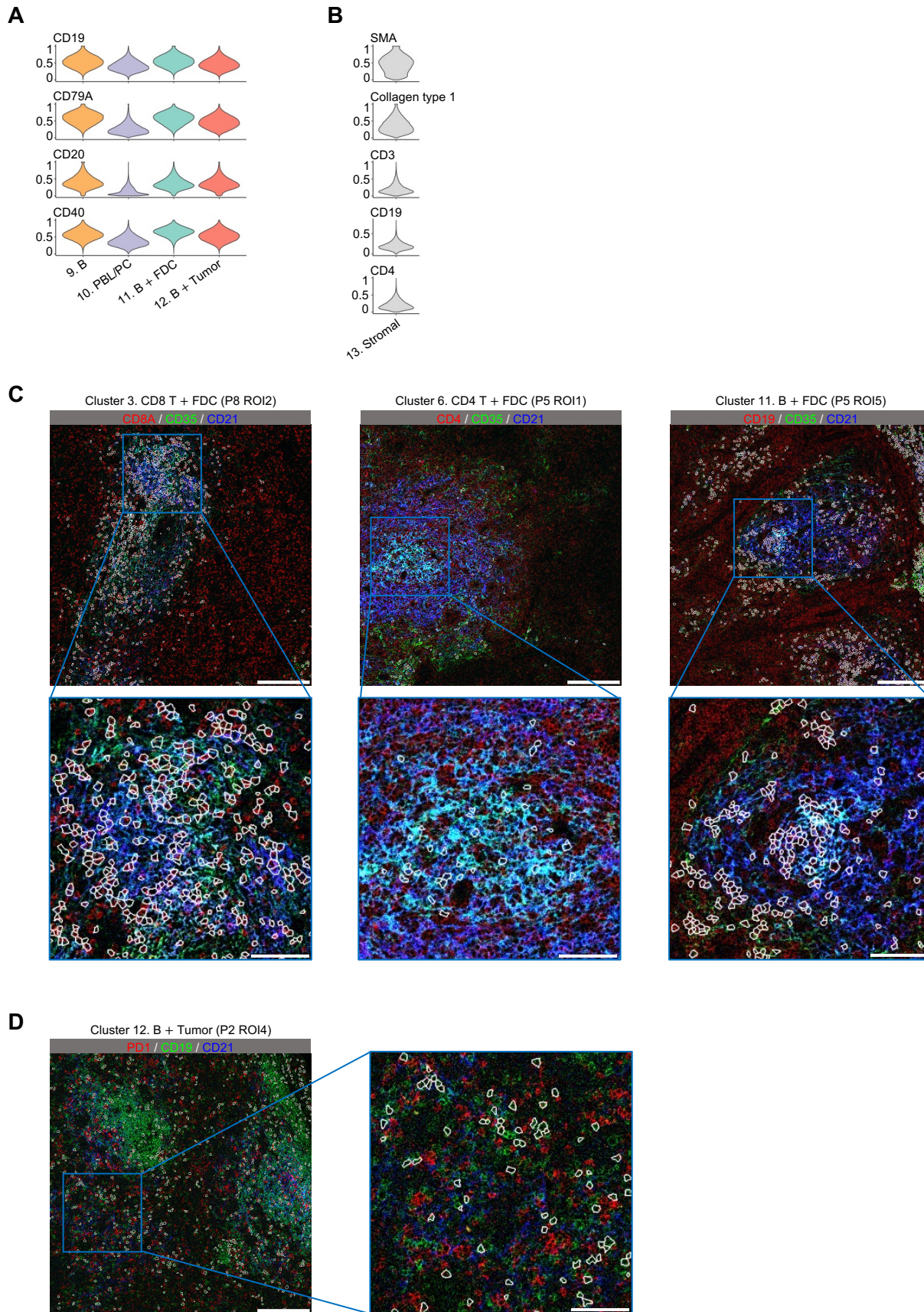


662 **Figure S17. Characteristics of subclusters of non-malignant PB T cells**

663 (A) Clone size of TCRs in non-malignant PB T cells. The number of cells expressing each
664 clonotype was defined as clone size and illustrated for each cell.

665 (B) TCR overlap analysis of non-malignant PB T cells, analyzed and illustrated for PB from
666 TFHL patients (upper right) and HDs (lower left), respectively.

Supplementary Figure 18



667 **Figure S18. Annotation of subclusters of non-malignant cells in spatial analysis**

668 (A) Violin plots of B-cell markers in B-cell clusters (clusters 9–12).

669 (B) Violin plots of stromal and lineage markers in a stromal-cell cluster (cluster 13).

670 (C) Representative IMC images of doublet clusters of FDCs and CD8⁺ T (cluster 3, left), CD4⁺
671 T (cluster 6, middle), and B (cluster 11, right) cells, colored according to expression levels of
672 markers for FDCs (CD21 and CD35) and each cell (CD8A, CD4, and CD19, respectively). Cells
673 belonging to each doublet cluster are outlined with white lines. ROI, region of interest; Scale bar,
674 300 μm (top) and 100 μm (bottom).

675 (D) Representative IMC images of doublet clusters of B and tumor cells (cluster 12) colored
676 according to expression levels of markers for B cells (CD19), tumor cells (PD1), and FDCs
677 (CD21). Cells belonging to each doublet cluster are outlined with white lines. Scale bar, 300 μm
678 (left) and 100 μm (right).

679 **Supplementary References**

- 680 1 Fujisawa M, Nguyen TB, Abe Y, Suehara Y, Fukumoto K, Suma S *et al.* Clonal
681 germinal center B cells function as a niche for T-cell lymphoma. *Blood* 2022; **140**:
682 1937–1950.
- 683 2 Wickham H. *ggplot2*. Springer International Publishing: Cham, 2016 doi:10.1007/978-3-
684 319-24277-4.
- 685 3 Wen W, Su W, Tang H, Le W, Zhang X, Zheng Y *et al.* Immune cell profiling of
686 COVID-19 patients in the recovery stage by single-cell sequencing. *Cell Discov* 2020; **6**:
687 31.
- 688 4 McCarthy DJ, Campbell KR, Lun ATL, Wills QF. Scater: pre-processing, quality
689 control, normalization and visualization of single-cell RNA-seq data in R.
690 *Bioinformatics* 2017; **33**: 1179–1186.
- 691 5 Villani A-C, Satija R, Reynolds G, Sarkizova S, Shekhar K, Fletcher J *et al.* Single-cell
692 RNA-seq reveals new types of human blood dendritic cells, monocytes, and progenitors.
693 *Science* 2017; **356**. doi:10.1126/science.aah4573.
- 694 6 Stuart T, Butler A, Hoffman P, Hafemeister C, Papalexi E, Mauck WM *et al.*
695 Comprehensive Integration of Single-Cell Data. *Cell* 2019; **177**: 1888-1902.e21.
- 696 7 Haghverdi L, Lun ATL, Morgan MD, Marioni JC. Batch effects in single-cell RNA-
697 sequencing data are corrected by matching mutual nearest neighbors. *Nat Biotechnol*
698 2018; **36**: 421–427.
- 699 8 Lavin Y, Kobayashi S, Leader A, Amir E-AD, Elefant N, Bigenwald C *et al.* Innate
700 Immune Landscape in Early Lung Adenocarcinoma by Paired Single-Cell Analyses. *Cell*
701 2017; **169**: 750-765.e17.
- 702 9 Cheng S, Li Z, Gao R, Xing B, Gao Y, Yang Y *et al.* A pan-cancer single-cell

703 transcriptional atlas of tumor infiltrating myeloid cells. *Cell* 2021; **184**: 792-809.e23.

704 10 Yang C, Siebert JR, Burns R, Gerbec ZJ, Bonacci B, Rymaszewski A *et al.*
705 Heterogeneity of human bone marrow and blood natural killer cells defined by single-
706 cell transcriptome. *Nat Commun* 2019; **10**: 3931.

707 11 Pizzolato G, Kaminski H, Tosolini M, Franchini D-M, Pont F, Martins F *et al.* Single-
708 cell RNA sequencing unveils the shared and the distinct cytotoxic hallmarks of human
709 TCRV δ 1 and TCRV δ 2 $\gamma\delta$ T lymphocytes. *Proc Natl Acad Sci U S A* 2019; **116**: 11906–
710 11915.

711 12 Germain P-L, Lun A, Garcia Meixide C, Macnair W, Robinson MD. Doublet
712 identification in single-cell sequencing data using scDbtFinder. *F1000Research* 2021;
713 **10**: 979.

714 13 Aran D, Looney AP, Liu L, Wu E, Fong V, Hsu A *et al.* Reference-based analysis of
715 lung single-cell sequencing reveals a transitional profibrotic macrophage. *Nat Immunol*
716 2019; **20**: 163–172.

717 14 Padovan E, Casorati G, Dellabona P, Meyer S, Brockhaus M, Lanzavecchia A.
718 Expression of two T cell receptor alpha chains: dual receptor T cells. *Science* 1993; **262**:
719 422–4.

720 15 Schuldt NJ, Binstadt BA. Dual TCR T Cells: Identity Crisis or Multitaskers? *J Immunol*
721 2019; **202**: 637–644.

722 16 Shi Z, Zhang Q, Yan H, Yang Y, Wang P, Zhang Y *et al.* More than one antibody of
723 individual B cells revealed by single-cell immune profiling. *Cell Discov* 2019; **5**: 64.

724 17 Brady BL, Steinel NC, Bassing CH. Antigen receptor allelic exclusion: an update and
725 reappraisal. *J Immunol* 2010; **185**: 3801–8.

726 18 ImmunoMind. immunarch: An R Package for Painless Bioinformatics Analysis of T-Cell

727 and B-Cell Immune Repertoires. Zenodo. 2019.

728 19 Finak G, McDavid A, Yajima M, Deng J, Gersuk V, Shalek AK *et al.* MAST: a flexible
729 statistical framework for assessing transcriptional changes and characterizing
730 heterogeneity in single-cell RNA sequencing data. *Genome Biol* 2015; **16**: 278.

731 20 Zhou Y, Zhou B, Pache L, Chang M, Khodabakhshi AH, Tanaseichuk O *et al.*
732 Metascope provides a biologist-oriented resource for the analysis of systems-level
733 datasets. *Nat Commun* 2019; **10**: 1523.

734 21 Subramanian A, Tamayo P, Mootha VK, Mukherjee S, Ebert BL, Gillette MA *et al.*
735 Gene set enrichment analysis: a knowledge-based approach for interpreting genome-
736 wide expression profiles. *Proc Natl Acad Sci U S A* 2005; **102**: 15545–50.

737 22 Hänzelmann S, Castelo R, Guinney J. GSEA: gene set variation analysis for microarray
738 and RNA-seq data. *BMC Bioinformatics* 2013; **14**: 7.

739 23 Robinson MD, McCarthy DJ, Smyth GK. edgeR: a Bioconductor package for
740 differential expression analysis of digital gene expression data. *Bioinformatics* 2010; **26**:
741 139–40.

742 24 McCarthy DJ, Chen Y, Smyth GK. Differential expression analysis of multifactor RNA-
743 Seq experiments with respect to biological variation. *Nucleic Acids Res* 2012; **40**: 4288–
744 97.

745 25 Kassambara A. rstatix:Pipe-Friendly Framework for Basic Statistical Tests. R package
746 version 0.7.0. <https://CRANR-project.org/package=rstatix> 2021.

747 26 Qiu X, Hill A, Packer J, Lin D, Ma Y-A, Trapnell C. Single-cell mRNA quantification
748 and differential analysis with Census. *Nat Methods* 2017; **14**: 309–315.

749 27 Cao J, Spielmann M, Qiu X, Huang X, Ibrahim DM, Hill AJ *et al.* The single-cell
750 transcriptional landscape of mammalian organogenesis. *Nature* 2019; **566**: 496–502.

751 28 Street K, Risso D, Fletcher RB, Das D, Ngai J, Yosef N *et al.* Slingshot: cell lineage and
752 pseudotime inference for single-cell transcriptomics. *BMC Genomics* 2018; **19**: 477.

753 29 Garcia-Alonso L, Handfield L-F, Roberts K, Nikolakopoulou K, Fernando RC, Gardner
754 L *et al.* Mapping the temporal and spatial dynamics of the human endometrium in vivo
755 and in vitro. *Nat Genet* 2021; **53**: 1698–1711.

756 30 Browaeys R, Saelens W, Saeys Y. NicheNet: modeling intercellular communication by
757 linking ligands to target genes. *Nat Methods* 2020; **17**: 159–162.

758 31 Makishima K, Suehara Y, Abe Y, Hattori K, Kusakabe M, Matsuoka R *et al.* Intratumor
759 heterogeneity of lymphoma identified by multiregion sequencing of autopsy samples.
760 *Cancer Sci* 2022; **113**: 362–364.

761 32 Abe Y, Sakata-Yanagimoto M, Fujisawa M, Miyoshi H, Suehara Y, Hattori K *et al.* A
762 single-cell atlas of non-haematopoietic cells in human lymph nodes and lymphoma
763 reveals a landscape of stromal remodelling. *Nat Cell Biol* 2022; **24**: 565–578.

764 33 Robinson JT, Thorvaldsdóttir H, Winckler W, Guttman M, Lander ES, Getz G *et al.*
765 Integrative genomics viewer. *Nat Biotechnol* 2011; **29**: 24–6.

766 34 McKenna A, Hanna M, Banks E, Sivachenko A, Cibulskis K, Kernytsky A *et al.* The
767 Genome Analysis Toolkit: a MapReduce framework for analyzing next-generation DNA
768 sequencing data. *Genome Res* 2010; **20**: 1297–303.

769 35 Petti AA, Williams SR, Miller CA, Fiddes IT, Srivatsan SN, Chen DY *et al.* A general
770 approach for detecting expressed mutations in AML cells using single cell RNA-
771 sequencing. *Nat Commun* 2019; **10**: 3660.

772 36 Tirosh I, Izar B, Prakadan SM, Wadsworth MH, Treacy D, Trombetta JJ *et al.* Dissecting
773 the multicellular ecosystem of metastatic melanoma by single-cell RNA-seq. *Science*
774 2016; **352**: 189–96.

775 37 Kurtenbach S, Cruz AM, Rodriguez DA, Durante MA, Harbour JW. Uphyloplot2:
776 visualizing phylogenetic trees from single-cell RNA-seq data. *BMC Genomics* 2021; **22**:
777 419.

778 38 Peng J, Sun B-F, Chen C-Y, Zhou J-Y, Chen Y-S, Chen H *et al.* Single-cell RNA-seq
779 highlights intra-tumoral heterogeneity and malignant progression in pancreatic ductal
780 adenocarcinoma. *Cell Res* 2019; **29**: 725–738.

781 39 Zanutelli VR, Bodenmiller B. ImcSegmentationPipeline: A pixel-classification based
782 multiplexed image segmentation pipeline. *Zenodo* 2022. doi:10.5281/zenodo.3841961.

783 40 Berg S, Kutra D, Kroeger T, Strahle CN, Kausler BX, Haubold C *et al.* ilastik:
784 interactive machine learning for (bio)image analysis. *Nat Methods* 2019; **16**: 1226–1232.

785 41 Stirling DR, Swain-Bowden MJ, Lucas AM, Carpenter AE, Cimini BA, Goodman A.
786 CellProfiler 4: improvements in speed, utility and usability. *BMC Bioinformatics* 2021;
787 **22**: 433.

788 42 Windhager J, Bodenmiller B, Eling N. An end-to-end workflow for multiplexed image
789 processing and analysis. *bioRxiv* 2021.

790 43 Eling N, Damond N, Hoch T, Bodenmiller B. Cytomapper: an R/bioconductor package
791 for visualisation of highly multiplexed imaging data. *Bioinformatics* 2020; **36**: 5706–8.

792 44 Sakaguchi S, Mikami N, Wing JB, Tanaka A, Ichiyama K, Ohkura N. Regulatory T
793 Cells and Human Disease. *Annu Rev Immunol* 2020; **38**: 541–566.

794 45 Bagaev D V., Vroomans RMA, Samir J, Stervbo U, Rius C, Dolton G *et al.* VDJdb in
795 2019: database extension, new analysis infrastructure and a T-cell receptor motif
796 compendium. *Nucleic Acids Res* 2020; **48**: D1057–D1062.

797 46 Swerdlow SH, Campo E, Pileri SA, Lee Harris N, Stein H, Siebert R *et al.* The 2016
798 revision of the World Health Organization classification of lymphoid neoplasms. *Blood*.

799 2016; **127**: 2375–2390.

800 47 Yabe M, Gao Q, Ozkaya N, Huet S, Lewis N, Pichardo JD *et al.* Bright PD-1 expression
801 by flow cytometry is a powerful tool for diagnosis and monitoring of
802 angioimmunoblastic T-cell lymphoma. *Blood Cancer J* 2020; **10**: 32.

803 48 Zhang L, Yu X, Zheng L, Zhang Y, Li Y, Fang Q *et al.* Lineage tracking reveals
804 dynamic relationships of T cells in colorectal cancer. *Nature* 2018; **564**: 268–272.

805 49 Maier B, Leader AM, Chen ST, Tung N, Chang C, LeBerichel J *et al.* A conserved
806 dendritic-cell regulatory program limits antitumour immunity. *Nature* 2020; **580**: 257–
807 262.